Broadband Spectrometer for Measuring the Low-Temperature Microwave Absorption of Unconventional Superconductors

by

Jake Stanley Bobowski

B.Sc., The University of Manitoba, 2002

A THESIS SUBMITTED IN PARTIAL FULFILMENT OF
THE REQUIREMENTS FOR THE DEGREE OF

MASTER OF SCIENCE

in

The Faculty of Graduate Studies

(Department of Physics and Astronomy)

We accept this thesis as conforming
to the required standard

THE UNIVERSITY OF BRITISH COLUMBIA

October 10, 2004

Library Authorization

In presenting this thesis in partial fulfillment of the requirements for an advanced degree at the University of British Columbia, I agree that the Library shall make it freely available for reference and study. I further agree that permission for extensive copying of this thesis for scholarly purposes may be granted by the head of my department or by his or her representatives. It is understood that copying or publication of this thesis for financial gain shall not be allowed without my written permission.

Jake Bobowski

Name of Author *(please print)*

10/10/2004

Date (dd/mm/yyyy)

Title of Thesis: Broadband Spectrometer for Measuring the Low-Temperature Microwave Absorption of Unconventional Superconductors

Degree: Master of Science Year: 2004

Department of Physics and Astronomy
The University of British Columbia
Vancouver, BC Canada

Abstract

A highly sensitive spectrometer has been designed and built to measure the ultra-low temperature surface resistance of unconventional superconducting single crystals continuously over a broad range of microwave frequencies. The technique uses bolometric detection to measure the temperature rise of samples that have been exposed to a microwave magnetic field. An in-situ normal metal reference sample is used to calibrate the field strength at the sample site and is vital to the success of the measurement.

This broadband technique has already been applied by researches at UBC to make detailed measurements of the conductivity spectrum of $YBa_2Cu_3O_{6+y}$ and have revealed, for the first time, the cusp-like line shape expected for a *d*-wave superconductor. Thus far these measurements have been limited to temperatures above 1 K and there remain several key issues regarding low-energy quasiparticle dynamics in these materials that this new spectrometer will address.

A new broadband apparatus has been designed to be used with a $^3He/^4He$ dilution refrigerator that can achieve base temperatures less than 50 mK. The main obstacle encountered in adapting this technique for use at lower temperatures is achieving the necessary temperature stability required to reliably perform the measurements. Low-pass thermal filters have been designed and constructed that will substantially suppress any temperature instabilities before they are able to reach the sample thermal stages. An equivalent circuit model was developed and implemented to numerically evaluate the filter performance.

This low-temperature microwave spectrometer will be used to uncover new physics regarding low-energy quasiparticle dynamics in $YBa_2Cu_3O_{6+y}$ and other materials, such as heavy fermion compounds, that is inaccessible by any other measurement technique.

Contents

List of Tables

List of Figures

Acknowledgements

First, I thank Walter Hardy and Doug Bonn for providing me with a stimulating project to work on over the past two years. I look forward to pursuing this line of research during my PhD. work. For sharing all his experience and wisdom in experimental low temperature physics I owe Walter a great deal of gratitude. I am also in debt to Doug for many useful discussions regarding the, at times puzzling, physics of unconventional superconductivity.

I am continually impressed with the genuine excitement shown by David Broun about all aspects of physics, from designing a new experiment to comparing the latest data with the newest theory. It has always been very inspiring to work alongside Dave. More than anyone, Pat Turner has guided me throughout the past 28 months. In addition to keeping me up to date with the latest music Pat has taught me a tremendous amount about the bolometry experiment. Pat's extreme patience has always been very appreciated.

I have also benefitted from the kindness and humour of Pinder Dosanjh. I am grateful to Ruixing Liang for providing such beautiful crystals, and for illuminating discussions regarding their growth and properties. I want to thank Darren Peets for his computer assistance and his interest in the development of South campus. It has been a pleasure to know Jen DeBenedictis , thanks for the climbing adventures. Richard Harris and Ahmed Hosseini have provided a friendly and supportive environment to work in.

I have Dan Beaton, Geoff Mullins, and Marty Kurylowicz to thank for many useful discussions regarding lab and course work. More importantly I want to thank them for the many discussions that were centred outside of physics. There are several friends outside the lab that I need to thank: Donovan, Tara, Karene, Hiro, Dominic, Greg, Sari, and Lara you have all contributed to make my time spent in Vancouver enjoyable.

Finally, I need to thank my family. In particular thank-you Auntie Joyce and Grannie Bobowski for providing a caring and warm atmosphere while I have been in Vancouver. To the family back in Winnipeg thanks for the continued support. Most importantly, I have always received constant love and encouragement from my parents, without which I never could have completed this work.

Part I

Thesis

Chapter 1

High T_C Superconductors and their Electrodynamics

1.1 A Brief History of Superconductivity

In 1911, shortly after helium was first liquified, Dutch physicist H. Kamerlingh Onnes of Leiden University discovered the first superconductor when he found that the resistance of mercury suddenly vanished when cooled below 4.15 K. In 1935 the brothers F. and H. London put forth a pair of phenomenological equations that described the two hallmark features of superconductivity, namely their perfect conductivity and the Meissner effect in which electromagnetic fields are expelled from the interior of the superconductor to within a penetration depth λ. A true microscopic description of superconductivity would have to wait until 1957 when Bardeen, Cooper, and Schrieffer offered their famous BCS theory. They showed that any attractive interaction between electrons, no matter how weak, results in an instability of the ground state Fermi sea against the formation of bound pairs of electrons. The electrons forming these so-called Cooper pairs have equal and opposite momentum and zero total spin. The mechanism for the required attractive interaction is the electron-phonon interaction. A simple picture is given by imagining an electron moving through a lattice of positive ions. The ions are attracted to the negative charge of the electron resulting in a small excess of positive charge which attracts a second electron forming a bound pair. Given the importance of the electron-phonon interaction it may not be surprising that metals with very low normal state resistivity, such as copper and gold, do not appear to exhibit superconductivity at any temperature whereas niobium and lead which are relatively poor conductors in the normal state have the highest superconducting transition temperatures of all the elements. Below the transition temperature T_c the electron system Bose-condenses into a condensate of Cooper pairs. The energy required to break a Cooper pair and create two quasiparticle excitations is $2\Delta(T)$ where $\Delta(T)$ is an energy gap and is zero above T_c. BCS theory is thought to be one of the most successful theories in condensed matter physics providing a truly microscopic picture of the mechanism driving superconductivity.

Since the time of Onnes' discovery other elements and certain metallic alloys have been found to superconduct at substantially higher temperatures. The steadily increasing values of T_c seemed to peak in 1973 when the alloy Nb_3Ge was found to superconduct at 23 K. In 1962 the first commercially available superconducting wire was fabricated from an alloy of niobium and titanium. By now magnets made from coils of superconducting wire have become commonplace. Also in 1962, as a graduate student at Cambridge University Brian D. Josephson predicted that in the absence

of an applied voltage a DC supercurrent would flow between two superconducting electrodes connected by a "weak link", such as a thin normal metal layer. In addition applying a voltage across the junction will give rise to an alternating current whose frequency is proportional to the voltage. Shortly after Josephson junctions were fabricated and Josephson's predictions verified. Josephson junctions have led to the development of superconducting quantum interference devices (SQUIDs) that are used as extremely sensitive magnetometer with noise levels as low as 3 $\mathrm{fT}/\sqrt{\mathrm{Hz}}$. In 1986 the field of superconductivity was reignited when Bednorz and Müller fabricated the first ceramic high-temperature superconductor (HTSC) $La_{1.85}Ba_{0.15}CuO_4$ with $T_c \approx 30$ K. [3]

1.2 Nineteen Eighty-Six

In the time since the discovery of Bednorz and Müller several other HTSCs have been made with transition temperatures well over 100 K. BCS theory in its original form does not apply to high-T_c materials and to this date no microscopic theory has been widely accepted. Electron pairing is still thought to occur, although the mechanism responsible for the pairing remains unclear. A large effort within the condensed matter physics community, both in theory and experiment, continues to be made to try better understand these materials.

The HTSC compounds that have attracted the most attention from researchers are $YBa_2Cu_3O_{6+y}$, $La_{2-x}Sr_xCuO_{4+\delta}$, and $Bi_2Sr_2Ca_{n-1}Cu_nO_{2n+6}$. All of these materials are layered cuprate perovskites which contain 2-dimensional copper oxide planes where the superconductivity is thought to reside. Of these materials $YBa_2Cu_3O_{6+y}$ (YBCO) has been one of the most widely studied due to its very high chemical purity and the relative ease with which it can be grown. The $YBa_2Cu_3O_6$ ($y = 0$) unit cell is tetragonal, however the fully doped $YBa_2Cu_3O_7$ ($y = 1$) has a slight orthorhombic distortion. This distortion can give rise to the formation of twins during sample growth which can be mechanically removed at a later time. Fig. 1.1 is a schematic drawing of one unit cell of fully doped $YBa_2Cu_3O_7$. The unit cell dimensions are $\hat{a} = 3.9198$ Å, $\hat{b} = 3.8849$ Å, and $\hat{c} = 11.6762$ Å. YBCO is a bilayer material having two CuO_2 planes per unit cell. A convenient way to dope charge carriers into the CuO_2 planes is to vary the oxygen content (from $y = 0$ to 1) in the so called CuO chains. The CuO chains run along the $\hat{b}$-direction with all of the oxygen sites filled in fully doped YBCO. Each excess oxygen atom in the chains removes one electron from its two neighbouring Cu^{1+} ions changing them to Cu^{2+}. The Cu atoms are prevented from giving up two electrons because the Cu^{3+} state is suppressed by a large on-site Coulomb repulsion in the Cu $3d$ shell. Chain fragments are formed when the chain oxygen sites of two or more neighbouring unit cells are filled. In such a case holes are formed in the CuO chains due to the deficiency of available electrons from the Cu atoms. These chain holes are partially filled with electrons from the CuO_2 planes and as a result hole carriers are introduced into the planes. Thus, it is both oxygen content and oxygen ordering that determines the number of holes introduced into the planes. The ordered phase that is of importance for this thesis is the ortho-II phase

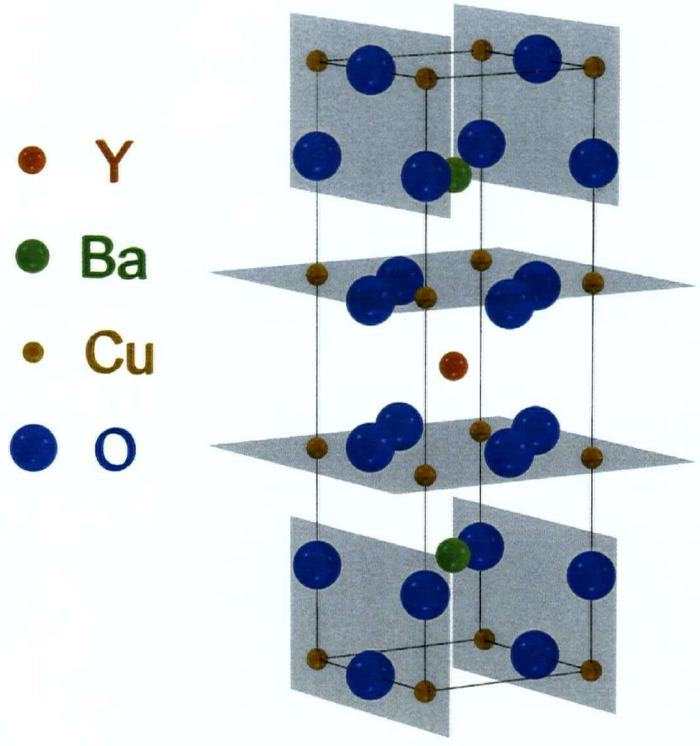

Figure 1.1: Schematic drawing of one unit cell of fully doped $YBa_2Cu_3O_7$. The CuO_2 planes are restricted to the *ab*-plane and are indicated by the horizontal shaded regions. The CuO chains run along the $\hat{b}$-direction and are highlighted by the vertical shaded regions. This figure was generated by and appears courtesy of Darren Peets.

which contains alternating full and empty chains and occurs at an oxygen content of $y = 0.5$.[1] For oxygen content near 6 ($y = 0$) YBCO is an antiferromagnetic insulator with a Néel temperature of 400 K. At an oxygen content of 6.33 there is a metal-insulator transition with a superconducting phase below a critical temperature T_c. YCBO has a maximum transition temperature of $T_c = 93$ K at an optimal doping of $y = 0.93$. [5]

The UBC group has benefitted greatly from the expertise of Dr. Ruixing Liang who produces the world's highest quality single crystals of YBCO. The crystals are grown using a self-flux method that has been described elsewhere [6, 7, 8]. If one hopes to probe the intrinsic properties of HTSCs it is essential to work with the highest quality samples available, accordingly the experimental work at UBC is performed almost exclusively using Dr. Liang's YBCO single crystals.

One fundamental difference between conventional and unconventional superconductors is the symmetry of the gap function $\Delta(\mathbf{k})$. Conventional superconductors are

[1] Inevitably a small amount of oxygen will reside in the empty chains so that the best ortho-II ordering is actually achieved with an oxygen content of $y = 0.52$ to ensure complete filling of the full chains [4].

characterized by the formation of electron pairs with zero total angular momentum (s-wave) which implies isotropic attractive forces between electrons in all spatial directions. These s-wave superconductors have a full gap surrounding the entire Fermi surface. In contrast, the electron pairing state of unconventional superconductors has finite angular momentum resulting from electron correlations caused by a large Coulomb repulsion at each Cu site in the CuO_2 planes. The superconducting ground state of the high-T_c cuprates is an antisymmetric spin singlet [9]. Group-theoretic calculations allow four distinct singlet pairing states for a single square CuO_2 plane [10]. By now the experimental evidence has conclusively shown that the gap symmetry of most HTSCs is $d_{x^2-y^2}$[2]. These d-wave superconductors have a gap maximum Δ_o along $\pm k_x$ and $\pm k_y$ and nodes 45° off axis in the ab-plane. Because HTSCs are strongly two-dimensional, little dispersion is expected in z-direction, and hence the nodes are line nodes that run along k_z. As noted above $YBa_2Cu_3O_{6+y}$ has a small orthorhombic distortion which results in an admixture of s- and d-wave pairing. The admixture is small and results in a slight distortion of the d-wave gap. The presence of the gap nodes allows for a finite quasiparticle density of states at all non-zero energies. The focus of this thesis is to present a novel technique that can be used to investigate low energy excitations through a measurement of the real part of the quasiparticle conductivity $\sigma_1(\omega, T)$ over a broad range of microwave frequencies and at temperatures accessible using a $^3He/^4He$ dilution refrigerator.

1.3 Microwave Surface Impedance

The surface impedance Z_s of a conductor in an electromagnetic field is defined as the ratio of tangential electric $\mathbf{E}$ to magnetic $\mathbf{H}$ fields at the conducting surface:

$$Z_s = \left(\frac{E_x}{H_y}\right)_{z=0} = R_s + iX_s, \tag{1.1}$$

where the surface of the conductor, which fills the half space $z < 0$, is at $z = 0$. R_s is the surface resistance and X_s is the surface reactance [11]. R_s is the important quantity for this work, and it will be shown in § 1.5 that it is responsible for power absorption by a conductor in an electromagnetic field. Provided we are in the limit of local electrodynamics, where for a superconductor, the coherence length ξ is much shorter than the magnetic penetration depth λ, it is appropriate to write the current density as $\mathbf{J} = \sigma\mathbf{E}$ where σ is the complex conductivity. Making use of this relation for the current density and Maxwell's equations for a region free of charge:

$$\nabla \cdot \mathbf{E} = 0, \tag{1.2a}$$

$$\nabla \times \mathbf{E} = -\mu\frac{\partial \mathbf{H}}{\partial t}, \tag{1.2b}$$

$$\nabla \cdot \mathbf{H} = 0, \tag{1.2c}$$

$$\nabla \times \mathbf{H} = \mathbf{J}, \tag{1.2d}$$

[2]See C. C. Tsuei and J. R. Kirtley for a complete review of the experimental evidence [9]

where $\mu \rightarrow \mu_o$ for a non-magnetic conductor, leads to the wave equations:

$$\nabla^2 \mathbf{E} = \mu_o \sigma \frac{\partial \mathbf{E}}{\partial t}, \tag{1.3a}$$

$$\nabla^2 \mathbf{H} = \mu_o \sigma \frac{\partial \mathbf{H}}{\partial t}. \tag{1.3b}$$

For our geometry with oscillating fields $\left(\propto \mathrm{e}^{\mathrm{i}\omega t}\right)$ applied perpendicular to the z-direction the wave equations become:

$$\frac{\mathrm{d}^2 E_x}{\mathrm{d}z^2} = \mathrm{i}\mu_o \sigma \omega E_x = k^2 E_x, \tag{1.4a}$$

$$\frac{\mathrm{d}^2 H_y}{\mathrm{d}z^2} = \mathrm{i}\mu_o \sigma \omega H_y = k^2 H_y, \tag{1.4b}$$

where the propagation constant, $k = \sqrt{\mathrm{i}\mu_o \sigma \omega}$ has been defined. These wave equations have the following solutions:

$$E_x(z,t) = E_{xo} \mathrm{e}^{-kz+\mathrm{i}\omega t}, \tag{1.5a}$$

$$H_y(z,t) = H_{yo} \mathrm{e}^{-kz+\mathrm{i}\omega t}. \tag{1.5b}$$

Substituting these solutions back into Maxwell's equations relates the coefficients of the two solutions, giving the surface impedance in terms of σ [12]:

$$Z_s = \frac{E_{xo}}{H_{yo}} = R_s + \mathrm{i}X_s = \sqrt{\frac{\mathrm{i}\mu_o \omega}{\sigma}}. \tag{1.6}$$

For a good metal conductor in the normal state, where $\sigma \gg \omega\epsilon$ (ϵ is the permittivity of the conductor), the conductivity is purely real [13] and:

$$R_s = X_s = \sqrt{\frac{\mu_o \omega}{2\sigma}}. \tag{1.7}$$

Using the definition of the classical skin depth $\delta = \sqrt{\frac{2}{\mu_o \omega \sigma}}$ one has:

$$R_s = \frac{\rho}{\delta}, \tag{1.8}$$

where $\rho = 1/\sigma$ is the resistivity of the metal.

In the general case σ is a complex quantity with $\sigma = \sigma_1 - \mathrm{i}\sigma_2$. Substituting σ into

Eq 1.6 leads to the following results for R_s and X_s:

$$R_s = \sqrt{\frac{\mu_o\omega(\sqrt{\sigma_1^2+\sigma_2^2}-\sigma_2)}{2(\sigma_1^2+\sigma_2^2)}}, \tag{1.9a}$$

$$X_s = \sqrt{\frac{\mu_o\omega}{2(\sigma_1^2+\sigma_2^2)}}\frac{\sigma_1}{\sqrt{\sqrt{\sigma_1^2+\sigma_2^2}-\sigma_2}}. \tag{1.9b}$$

In §1.4 it will be shown that in the superconducting state, for not too high frequencies, $\sigma_2 \gg \sigma_1$, in which case the above equations can be approximated as:

$$R_s \approx \frac{\sigma_1}{2\sigma_2}\sqrt{\frac{\mu_o\omega}{\sigma_2}}, \tag{1.10a}$$

$$X_s \approx \sqrt{\frac{\mu_o\omega}{\sigma_2}}. \tag{1.10b}$$

Note that in the approximation $\sigma \approx -i\sigma_2$ the propagation constant becomes $k \approx \sqrt{\mu_o\omega\sigma_2} \equiv 1/\lambda$, which when substituted back into Eqs. 1.5 lead to solutions that exponentially decay over a length scale given by λ, called the magnetic penetration depth. When written in terms of λ rather than σ_2 Eqs. 1.10 become:

$$R_s(\omega,T) \approx \frac{1}{2}\mu_o^2\omega^2\lambda^3(T)\,\sigma_1(\omega,T), \tag{1.11a}$$

$$X_s(\omega,T) \approx \mu_o\omega\lambda(T), \tag{1.11b}$$

where the explicit frequency and temperature dependencies have been put in. These are very useful approximate forms that one often refers to when doing simple data analysis. Notice that measurements of both $R_s(\omega,T)$ and $\lambda(T)$ are required to extract the values of $\sigma_1(\omega,T)$.

1.4 London Equations and the Two Fluid Model

The starting point for this section is the well known Drude model where one writes a classical equation of motion for conduction electrons in a conductor:

$$m\frac{\mathrm{d}\mathbf{v}}{\mathrm{d}t} = e\mathbf{E} - m\frac{\mathbf{v}}{\tau}, \tag{1.12}$$

where m is the electron mass, $\mathbf{v}$ is the average drift velocity of the electrons, $\mathbf{E}$ is an externally applied electric field, and τ is a phenomenological relaxation time. The probability that an electron will experience a scattering event in the time interval $\mathrm{d}t$ is given by $\mathrm{d}t/\tau$. In a normal metal equilibrium is reached when $\mathbf{v} = e\mathbf{E}\tau/m$ so that the current density $\mathbf{J} = ne\mathbf{v} = (ne^2\tau/m)\,\mathbf{E}$ takes on the familiar form of Ohm's law $J = \sigma\mathbf{E}$ with $\sigma = ne^2\tau/m$.

If the perfect conductivity of a superconductor can be represented by allowing the

relaxation time $\tau \rightarrow \infty$ then the super-current density obeys:

$$\frac{\mathrm{d}\mathbf{J}_s}{\mathrm{d}t} = \frac{n_s e^2}{m^\star}\mathbf{E}, \tag{1.13}$$

which is one way of forming the first London equation. In the above equation the subscript s indicates that the electrons described by this equation are superconducting electrons and $m^\star$ is the mass of the superconducting charge carriers. Eq. 1.13 implies that any applied electric field accelerates electrons rather than sustaining a velocity against a resistance given by Ohm's law.

London's second equation cannot be obtained by a classical argument and hence we appeal to a quantum one. In the absence of an applied field the ground state of the system has zero net canonical momentum:

$$< \mathbf{p} >=< m^\star \mathbf{v} + e\mathbf{A} >= 0, \tag{1.14}$$

where $\mathbf{A}$ is the vector potential. Provided the system remains in its ground state in the presence of a field the electrons will be accelerated to a velocity $< \mathbf{v}_s >= -e\mathbf{A}/m^\star$ and current density is given by:

$$\mathbf{J}_s = n_s e \mathbf{v}_s = -\frac{n_s e^2 \mathbf{A}}{m^\star}. \tag{1.15}$$

Taking the time derivative of this expression reproduces Eq. 1.13 and taking the curl leads to:

$$-\nabla \times \mathbf{J_s} = \nabla^2 \mathbf{H} = \frac{\mathbf{H}}{\lambda_L^2}, \tag{1.16}$$

where λ_L is the London penetration depth defined as $\lambda_L^{-2} = \mu_o n_s e^2/m^\star$. Eq. 1.16 is the second London equation and describes the Meissner effect in which magnetic fields are exponentially screened from the interior of the superconductor over a distance given by λ_L. As will be seen shortly the London penetration depth can differ from the magnetic penetration depth λ met in §1.3.

Returning to Eq. 1.12 and solving for $\sigma = \sigma_1 - \mathrm{i}\sigma_2$ assuming a harmonic time dependence for the electric field yields:

$$\sigma_1 = \sigma_o \frac{1}{1+\omega^2\tau^2}, \tag{1.17a}$$

$$\sigma_2 = \sigma_o \frac{\omega\tau}{1+\omega^2\tau^2}, \tag{1.17b}$$

$$\sigma_o = \frac{ne^2\tau}{m^\star}. \tag{1.17c}$$

Integrating $\sigma_1(\omega)$ over all frequencies gives a result that is independent of τ and ω,

$$\int_0^\infty \sigma_1(\omega)\,\mathrm{d}\omega = \frac{\pi}{2}\frac{ne^2}{m^\star}. \tag{1.18}$$

Eq. 1.18 is very general oscillator strength sum rule and is derived from a Kramers-Krönig transformation relating the real and imaginary parts of the causal response function $\sigma(\omega)$ in Appendix A.

In the generalized two fluid model the total conductivity is described as coming from two parallel and independent sources, one source is due to normal electrons and the other is due to the superconducting electrons, hence:

$$\sigma(\omega) = (\sigma_{1n}(\omega) - i\sigma_{2n}(\omega)) + (\sigma_{1s}(\omega) - i\sigma_{2s}(\omega)). \tag{1.19}$$

The total electron density $ne^2/m^\star$ is temperature independent and equal to the sum of the normalfluid density $n_n e^2/m^\star$ and the superfluid density $n_s e^2/m^\star$. In the clean limit all of the charge carriers condense into the superconducting ground state at $T = 0$ such that:

$$\frac{ne^2}{m^\star} = \frac{n_s e^2}{m^\star}(T=0) = \frac{n_n e^2}{m^\star}(T) + \frac{n_s e^2}{m^\star}(T). \tag{1.20}$$

Allowing $\tau_s \to \infty$ one finds from Eq. 1.17a that σ_{1s} becomes a δ-function at zero frequency. This δ-function represents the perfect DC conductivity of a superconductor and its coefficient is set by Eq. 1.18:

$$\sigma_{1s}(\omega) = \frac{\pi}{2}\frac{n_s e^2}{m^\star}\delta(\omega). \tag{1.21}$$

Thus at nonzero frequency σ_s is strictly determined by σ_{2s}. In the same limit ($\tau_s \to \infty$) σ_{2s} becomes:

$$\sigma_{2s} = \frac{n_s e^2}{m^\star \omega} = \frac{1}{\mu_o \omega \lambda_L^2(T)}. \tag{1.22}$$

Recalling our definition of the magnetic penetration depth $\lambda^2 = 1/\mu_o\omega\sigma_2$ points out that a measurement of λ will differ from $\lambda_L^2 = 1/\mu_o\omega\sigma_{2s}$ if there is significant contribution to σ_2 from σ_{2n}. When σ_{2n} makes a significant contribution to the total conductivity the normalfluid electrons play a role in screening electromagnetic fields, whereas the London penetration depth only takes into account screening by the superfluid.

Eq. 1.18 shows that the total integrated quasiparticle conductivity, σ_{1n}, is a measure of the normal fluid density, n_n:

$$\frac{n_n e^2}{m^\star}(T) = \frac{2}{\pi}\int_0^\infty \sigma_{1n}(\omega, T)\,d\omega, \tag{1.23}$$

and provided $\sigma_{2s} \gg \sigma_{2n}$ a measurement of the magnetic penetration depth can yield the superfluid density:

$$\frac{n_s e^2}{m^\star}(T) \approx \frac{1}{\mu_o}\frac{1}{\lambda^2(T)}. \tag{1.24}$$

The two preceding equations together with Eq: 1.20 require that oscillator strength lost in the superfluid density, from an increase in temperature for example, must

reappear as an increase in the integrated quasiparticle conductivity. Thus we have a valuable quantitative tool to test if all of the oscillator strength residing in the normal fluid is captured in the frequency range of our measured $\sigma_{1n}(\omega, T)$.

1.5 Power Absorption

The experiment presented in this thesis exposes conductors to microwave magnetic field and indirectly measures the power they absorb. In this section we calculate an expression for the power absorbed by the samples from the electromagnetic field. The power P absorbed per unit area A is given by:

$$\frac{\mathrm{d}P}{\mathrm{d}A} = \frac{1}{2}\mathrm{Re}\left[\mathbf{n}\cdot\mathbf{S}\right] \tag{1.25}$$

where $\mathbf{S} = \mathbf{E}\times\mathbf{H}^*$ is the Poynting vector and $\mathbf{n}$ is an outward unit vector normal to the surface of the conductor [14]. For the geometry adopted in §1.3 in which the conductor fills the half space $z < 0$ with the magnetic field applied along the y-direction, Eq. 1.25 reduces to:

$$\frac{\mathrm{d}P}{\mathrm{d}A} = \frac{1}{2}\mathrm{Re}\left[E_{xo}H_{yo}\right] = \frac{1}{2}\mathrm{Re}\left[Z_s H_{yo}^2\right] = \frac{1}{2}R_s H_{yo}^2. \tag{1.26}$$

Provided H_{yo} is uniform over the surface of the conductor the power absorbed is:

$$P = \frac{1}{2}R_s H_{surf}^2 A, \tag{1.27}$$

where H_{surf} is the applied magnetic at the surface of the conductor.

Chapter 2

Experiment Design and Measurement Technique

2.1 Motivation

The experiment developed during this thesis work was designed to measure the absolute surface resistance of high quality superconducting single crystals over a broad range of microwave frequencies. A typical sample is a thin (20 μm) platelet with a 1 mm^2 surface area. Because the samples are small and have such low loss, probing their surface impedance is technically challenging. At microwave frequencies cavity-perturbation techniques have been successful in measuring both components of Z_s [11, 15]. In such experiments the samples are loaded into a resonant cavity and changes in the resonant frequency and quality factor of the cavity are measured to yield the sample absorption and penetration depth respectively. These techniques, while extremely useful, are limited in the sense that each resonator works only at one fixed frequency, thus requiring multiple apparatuses to construct a coarse spectrum of data such as that produced by the UBC group in 1999 [16].

Here a non-resonant bolometric technique is described that is capable of measuring the low-temperature absorption of unconventional superconductors continuously over a broad range of microwave frequencies. The samples are weakly connected to a base temperature and exposed to microwave magnetic field whose frequency can be continuously varied. As the sample absorbs microwave power its temperature increases and this change in temperature is measured as a function of frequency using a resistance bolometer. This measurement is then used to extract the frequency dependent surface resistance $R_s(\omega, T)$. This experimental technique has already been employed by Patrick Turner and the UBC group with enormous success [1]. In particular two impressive results have recently been published. The first is an investigation of the frequency dependence of the a- and b-axis quasiparticle conductivity $\sigma_1(\omega, T)$ of $YBa_2Cu_3O_{6+y}$ from 200 MHz to 22 GHz [17]. The second is a novel method for measuring the absolute penetration depth of $YBa_2Cu_3O_{6+y}$ in the $T \rightarrow 0$ limit at several dopings [18].

Thus far, measurements made using this broadband bolometric technique have been performed in a pumped ^{4}He bath which achieves a base temperature of ~ 1.2 K. The focus of this present and ongoing work is to adapt this experiment for use with a ^{3}He/^{4}He dilution refrigerator which can reach temperatures below 50 mK. The main experimental obstacle in running this experiment at these low temperatures is avoiding temperature instabilities that can result in spurious signals. This issue is addressed in chapter 5. A sample of some of the exciting measurements we intend to

perform and unanswered questions we hope to probe using this new design are discussed in chapter 6. The remainder of the present chapter gives a detailed description of the design and operation of the experiment.

2.2 Design

The body of the experiment is a 6.6 mm long rectangular coaxial line kept at low temperature inside a cryostat. The exterior of the body is a copper block with a rectangular chamber that forms the outer conductor of the transmission line. The interior of the body contains a flat, broad beryllium-copper rectangular inner conductor that is centred in the chamber of the outer conductor. The centre conductor is shorted to the outer conductor via an end-wall. Fig. 2.1 is a schematic cross-section of the rectangular transmission line. A dimensioned scale drawing of the rectangular

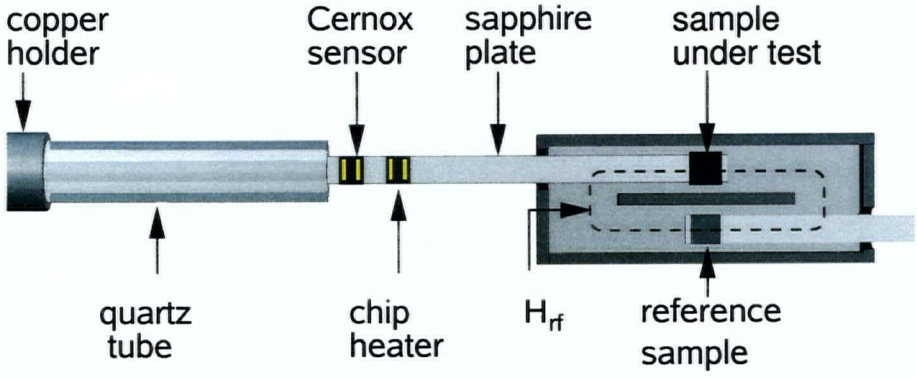

Figure 2.1: Schematic cross-section of the terminated coaxial line region showing the sample and reference materials suspended on sapphire plates in symmetric locations in the rf magnetic field. Each sapphire plate is equipped with a heater and a temperature sensor and is isolated from ^{4}He bath via a thermal weak link. This figure appears courtesy of Patrick Turner and is taken from reference [1].

coaxial line used in this thesis is shown in Fig. 2.2.

The outer and inner conductors of the experiment body are in turn fixed to the outer and inner conductors of a standard 0.141 in. cylindrical semi-rigid coaxial line[1] which runs from room temperature to the waveguide body. The inner conductor of the cylindrical transmission line is inserted into a small hole drilled into the centre conductor of the rectangular coaxial line. The surfaces of the objects making physical contact were first gold plated using electroplating pens to promote good electrical contact. Ultimately a contact resistance of 6 mΩ was achieved. The outer conductor of the cylindrical transmission line is stainless steel, chosen for its low thermal conductivity, and the inner conductor is silver plated copper weld, chosen for its low

[1]The coaxial cable used was UT-141-SS from Micro-Coax.

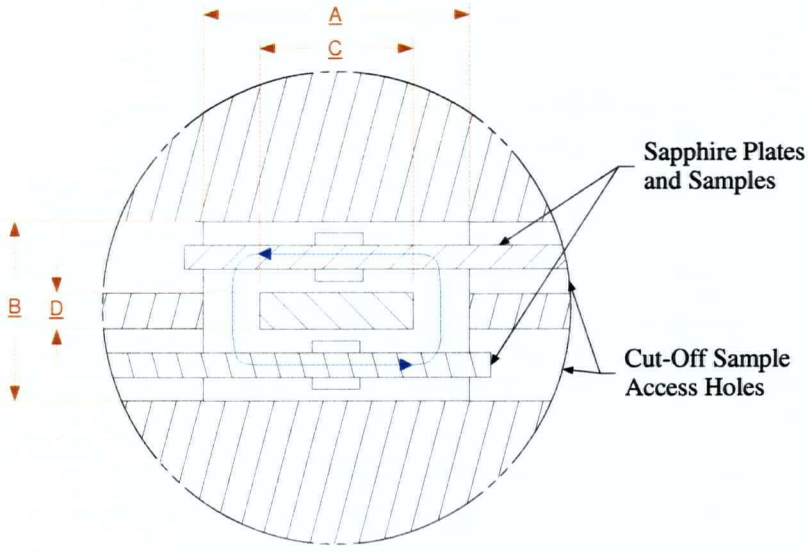

Figure 2.2: Scale drawing of a cross-section of the rectangular waveguide structure. The labelled dimensions are: A=5.64 mm, B=3.76 mm, C=3.25 mm, and D=0.76 mm. Each of the two sapphire plates supports a sample centred between the inner and outer conductors of the transmission line. The blue line represents the TEM magnetic field looping around and centre conductor in the plane of the page.

loss. Microwaves are supplied using an Hewlett Packard 83630A 10 MHz to 26.5 GHz synthesized sweeper and propagate down the semi-rigid coaxial cable and into the rectangular waveguide structure. This configuration, when operated in the TEM mode, produces magnetic fields that loop symmetrically around the inner conductor, see the blue line in Fig. 2.2. The various modes that can propagate in the rectangular structure are discussed in detail in Section 3.1. An estimate of the magnitude of the magnetic field H at the sample sites can be made using Ampere's Law:

$$\oint \mathbf{H} \cdot \mathrm{d}\mathbf{s} = i_{encl}, \tag{2.1}$$

where i_{encl} is the current enclosed by the Amperean loop. Choosing the path shown in Fig. 2.2 and assuming that H is constant everywhere on that path gives $H = i_{encl}/s$, where s is the circumference of the loop. One now has to make an estimate of the power P delivered to the waveguide to calculate the current $i_{enlc} = \sqrt{P/z_o}$. Estimating this power proves to be rather difficult, because although the impedance of the rectangular coaxial line is designed to match to that of the cylindrical coaxial cable ($z_o = 50\ \Omega$) a non-negligible reflection is still possible at that connection. Furthermore, some of the incident power will be dissipated due to losses in the cylindrical transmission line used to deliver microwaves to the waveguide. The cylindrical coaxial line goes from room temperature to $\sim$ 1.2 K so that the actual loss per foot is

difficult to determine despite the specifications supplied by the manufacturer. Nevertheless, the insertion loss specifications at 20° celsius are 0.25 dB/ft. at 1 GHz and 1.26 dB/ft. at 20 GHz. A continuous 4 ft. length of cable was used in the experiment so that a typical incident power of 22 dBm is reduced to 21 dBm = 126 mW and 17 dBm = 50 mW at the sample site for frequencies of 1 GHz and 20 GHz respectively. These powers correspond to currents of $i_{encl}^{1GHz} = 50$ mA and $i_{encl}^{20GHz} = 32$ mA resulting in $H^{1GHz} = 3.7$ Am^{-1} = 0.046 Oe and $H^{20GHz} = 2.4$ Am^{-1} = 0.030 Oe.

Samples are held very near the end-wall of the experiment body where there is an electric field node and a magnetic field anti-node and thus are exposed to predominately magnetic fields. The samples are held in place by 0.850 in. long sapphire plates (0.020 in. wide and 0.004 in. thick) whose presence has little perturbing effect on the microwave field. The sapphire plates are fed through 1/16 in. diameter cutoff holes in waveguide body that do not allow any modes to propagate out of the cavity below 145 GHz (see Figs. 2.1 and 2.2).

The last 15 cm of the cylindrical coaxial cable leading to the waveguide has been made superconducting in order to reduce heating near the experiment body due to resistive losses. Any excess heat can change the sensitivity of the measurement or provide spurious signals. To make the superconducting coaxial line a 15 cm section was disassembled, then the interior of the outer conductor was coated with 50/50 PbSn solder, which is superconducting below 7 K. The cable was then reassembled with a new stainless steel inner conductor which was also PbSn coated. In addition, it can be advantageous to construct the waveguide structure from superconducting material to minimize rf absorption, but was avoided here to allow for the possibility of performing measurements with an externally applied magnetic field. The cold end of the cylindrical transmission line has also been thermally anchored to the ^{4}He bath in an attempt to extract any excess heat.

2.3 Measurement Technique

This experiment gives a direct measurement of the power absorbed by a conductor in a microwave magnetic field. Recall Eq. 1.27 from §1.5 that the power is given by:

$$P = R_s H^2 A, \tag{2.2}$$

where A is the area of one broad face of the sample. The factor of 1/2 is absent because in the experiment both faces of the sample are exposed to the field thereby doubling the effective area A. Our experimental geometry has two independent sites on either side of the inner conductor that experience identical magnetic fields when the TEM mode is the only propagating mode (see the two sample sites in Fig. 2.2). This important fact allows us to simultaneously measure the power absorbed by two different conducting samples. One of the samples is a normal metal used as a power meter and from hereon is referred to as the reference sample. The other sample can be any conducting material, high temperature superconductor, heavy fermion, normal metal, ... and is the sample being investigated. Because the reference sample is a

normal metal its surface resistance is well understood and given by classical skin-effect relation introduced in §1.3:

$$R_s^{ref} = \frac{\rho}{\delta} = \sqrt{\frac{\mu_o \omega \rho}{2}}. \tag{2.3}$$

The reference samples used in these experiments are silver:gold (70:30 at. %) alloys and have a temperature independent resistivity of $5.28 \pm 0.3\ \mu\Omega m$ below 20 K [1]. An alloy reference sample is used to ensure that the electrodynamics remain local so that there is no contribution to the surface resistance from the anomalous skin effect.

Taking the ratio of the power absorbed by the two samples leaves the following simple expression:

$$\frac{P^{sam}}{P^{ref}} = \frac{R_s^{sam}}{R_s^{ref}} \frac{A^{sam}}{A^{ref}}, \tag{2.4}$$

where the sample of interest has been labelled with the superscript *sam* and the factor of H^2 has dropped out because it is identical for the two sample sites. P^{sam}, P^{ref}, A^{sam}, A^{ref}, and R_s^{ref} are all known quantities and hence R_s^{sam} is easily determined. All that remains is to describe how the powers absorbed by the samples are measured.

The samples are secured to sapphire plates using a small amount of Dow Corning high vacuum silicone grease, which ensures good thermal contact and allows easy installation and removal of the samples. These sapphire plates have very short thermal time constants and are considered to be isothermal stages. In addition to providing sample support, each sapphire plate is equipped with a chip heater and a temperature sensor. The heater and bolometer are fixed to the sapphire plate using GE varnish ensuring good thermal contact. The chip heater has a nearly temperature independent resistance of 1500 Ω and heats the sapphire stage when current is passed through it. The bolometer is a Lakeshore Cernox 1050 resistive thermometer that has a dimensionless sensitivity $|(T/R)(\mathrm{d}R/\mathrm{d}T)| \simeq 2$ over the temperature range 1 to 100 K. Each sapphire stage is connected to the base temperature via a weak thermal link having thermal conductance, G. For the sample stage a 12.1 mm long quartz tube with inner and outer diameters of 0.635 and 1.2 mm respectively was chosen as the thermal weak link. One end of the sapphire plate slides 1 mm deep into the quartz tube and is held in place with a small amount of Emerson & Cuming Stycast 1266 epoxy. The bolometer and heater are each equipped with a pair of 0.002 in. diameter bare NbTi superconducting leads, chosen for there low thermal conductivity, which run along the length of the quartz tube. The superconducting wires are thermally anchored to the quartz using GE varnish. A four wire resistance measurement is made from the free ends of the superconducting wires for both the Cernox detector and heater. A schematic drawing of the sample thermal stage is shown in Fig. 2.3 and Fig. 2.4 is a digital photo of the actual thermal stage. The reference stage is similar in construction to the sample stage, except that in place of the quartz we use a stainless steel tube. Because the reference sample is a normal metal and has a large surface resistance compared to a typical superconducting sample, much less sensitivity is required from the reference stage to acquire reasonable signal levels. The design criterion was to make the thermal conductance of the stainless steel tube ten times

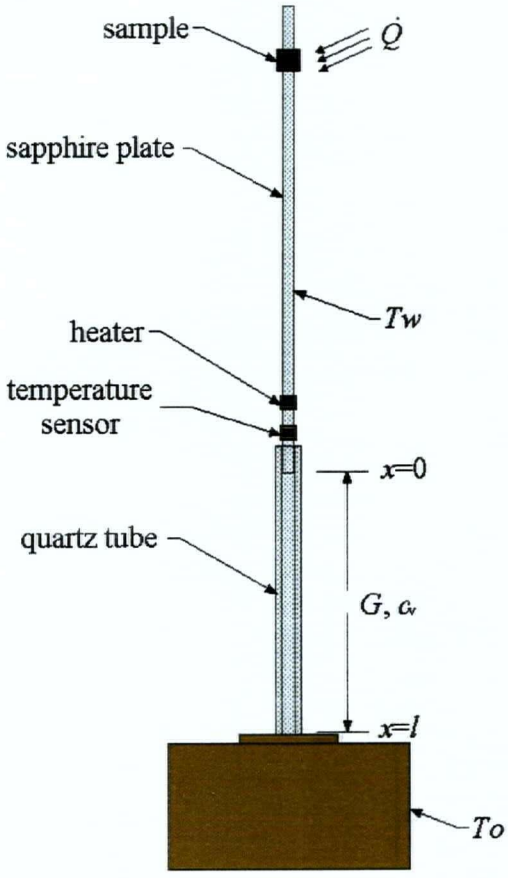

Figure 2.3: Schematic drawing of one of the sample thermal stage. The sample absorbs microwave power $\dot{Q}$, T_w and T_o are the temperatures of the sapphire plate and base respectively and G and c_v are the thermal conductance and specific heat of the quartz tube which has length l.

that of the quartz tube at a temperature of 1 K. Ultimately, the stainless steel used has an O.D. = 1.19 mm, I.D. = 0.90 mm, and a length of 2.54 mm. The electrical leads used on the reference stage are 0.003 in. diameter insulated manganin wires. The thermal conductance and heat capacity of these wires are negligible compared to those of the stainless steel tube, thus the thermal time constant of the reference stage is solely determined by the stainless steel.

When the reference sample absorbs power from the magnetic field it heats up, and the change in temperature is detected by the Cernox temperature sensor. The temperature change ΔT of the sample is related to the thermal conductance of the weak link in the following way:

$$\Delta T = \frac{P}{G}. \tag{2.5}$$

In practice the microwave power is modulated at low frequency ($\sim$ 1 Hz) causing a low frequency oscillation in the temperature of the samples. The short thermal

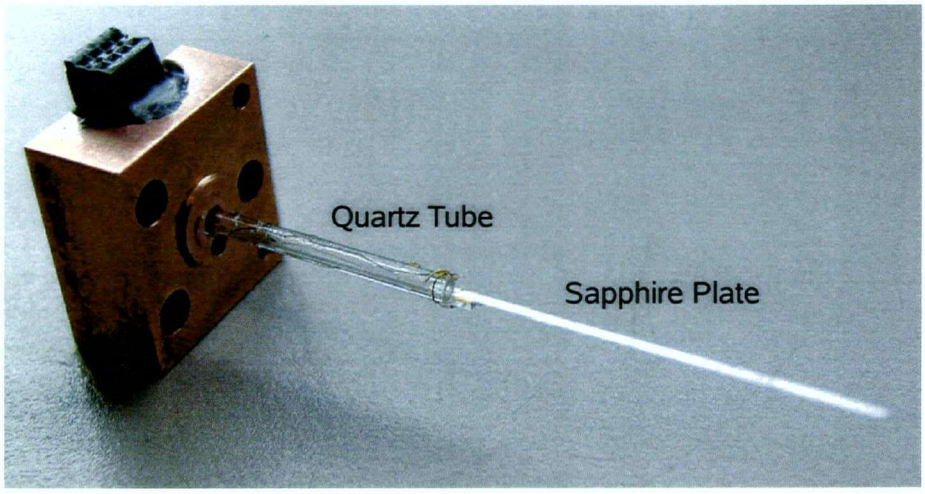

Figure 2.4: Digital photograph of the sample thermal stage.

time constant of the sapphire plate ensures that the change in sample temperature is detected by the bolometer on a time scale much shorter than the modulation period. A Stanford Research 850 Lock-in detector is used to synchronously detect this temperature oscillation as a change in the voltage across the bolometer. The samples studied are typically very high purity high temperature superconducting single crystals that can have a very small surface resistance (for example $R_s = 1\ \mu\Omega$ at 1 GHz, 1 K). Therefore the signals to be detected by the lock-in amplifier can be very small and easily swamped by external interference. For this reason the AC voltages from the sample bolometer are amplified by 10^4 within a bias box before being transmitted to the lock-in detector through an optical isolation stage to break ground loops. The signals from the reference stage are large enough that additional amplification is not required. The 1 Hz AC voltage from the bias box is proportional to the amplitude of the variation in the Cernox resistance. A method for converting this voltage to the absolute power absorbed by the sample is needed and a simple way of determining the necessary calibration factor has been developed. With no microwaves present, one can mimic the sample temperature fluctuation by passing a 1 Hz current i_H through the chip heater with resistance R_H. Then the Cernox response can be measured for a known power ($P = i_H^2 R_H$). Because the sensitivity (i.e. the thermal conductance) of the thermal weak link is temperature dependent, a calibration factor needs to be determined separately for all temperatures. The temperature of the sapphire stage is set by passing a small ($\sim 1 - 1000\ \mu A$) bias current through the Cernox detector, allowing frequency sweeps to be performed at temperatures ranging from 1.2-10 K. This method of setting the temperature maximizes the sensitivity of the measurement. A detailed calculation of the minimum detectable power is given in §4.3.

2.4 Thermal Filtering

The issue of thermal filtering is an important one in the design of this experiment because the measured signal is a periodic temperature modulation that must be carefully separated from other spurious temperature fluctuations. A semi-rigid coaxial line is used to transmit high power microwaves to the rectangular coaxial line which can result in fluctuations of the waveguide body temperature. These temperature fluctuations cannot be permitted to reach either the reference or sample stage. Although temperature fluctuations of the coaxial cable have been minimized through heat sinking and by making the last 15 cm superconducting, further thermal filtering was deemed necessary, specifically, low pass thermal filters have been placed between the waveguide body and the thermal stages.

The thermal stages are connected to the waveguide body through a length of Vespel SP-22 [19] tube which has been thermally anchored to the liquid ^{4}He bath using copper blocks and silver wire. Vespel is a graphite based material that has a low thermal conductivity and is easily machined. The vespel acts as a thermal resistance whereas the copper blocks have a large heat capacity and very low thermal resistance. Refer to Fig. 2.5.

To analyze heat transfer in the experiment an equivalent electrical circuit is used to model the final design. In this model, voltage becomes temperature, resistance becomes inverse thermal conductance, capacitance becomes heat capacity, and current becomes thermal power. There is, however, an important distinction that must be made between this model and conventional circuit analysis. This distinction can be seen most easily be recalling the definition of thermal conductance, G:

$$G = \frac{1}{|T_2 - T_1|}\frac{A}{l}\int_{T_1}^{T_2} \kappa(T)\mathrm{d}T, \tag{2.6}$$

where T_1 and T_2 are the temperatures at opposite ends of a material length l and cross-sectional area A and $\kappa(T)$ is the temperature dependent thermal conductivity. Clearly the thermal conductance depends on the temperature difference across the material, whereas in conventional circuit analysis a resistor's value does not depend on the voltage difference across it. Provided that the temperature difference across the material is not too large the thermal conductance can be approximated as $G \approx (A/l)\kappa(\bar{T})$ where $\bar{T} = (T_1 + T_2)/2$ is the average temperature. When this approximation is valid the thermal conductance of the material no longer directly depends on the temperature difference across it and analyzing the equivalent thermal circuits proceeds as in conventional circuit analysis.

Here again are the replacements used by the model:

$$v \rightarrow T,\ R \rightarrow G^{-1},\ C \rightarrow \rho V c_v,\ i \rightarrow P. \tag{2.7}$$

The lower case symbols v and i represent AC voltage and current respectively, V is volume and c_v is specific heat per unit mass. Now all that is left is to generate the equivalent circuit and analyze it using the familiar Kirchhoff voltage and current

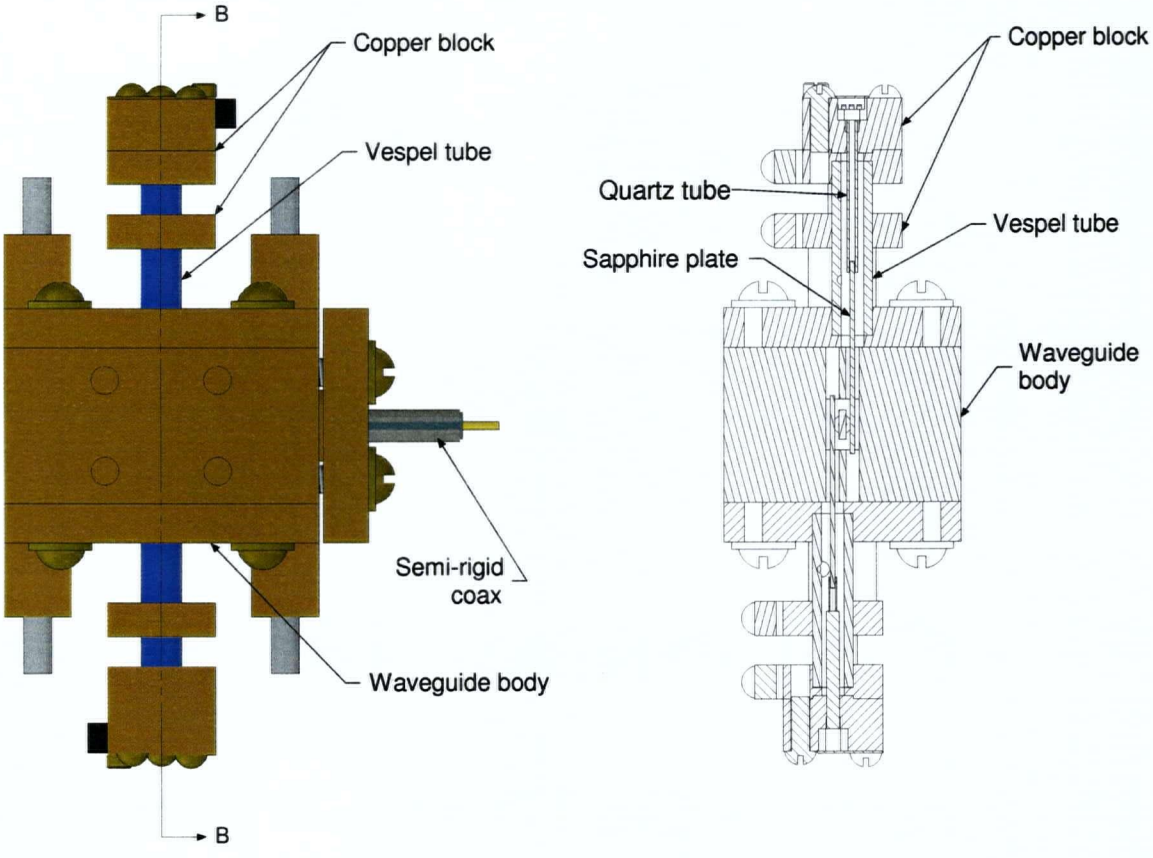

Figure 2.5: Schematic drawing of the experimental setup. Right: Overhead view of the waveguide body and the two copper/vespel filters. Left: Cross-sectional view showing the thermal stages down the centre of the vespel tubes.

laws. Fig. 2.6 shows the equivalent circuit for one of the low-pass copper/vespel filters. This circuit represents two cascaded low-pass filters such that:

$$\left|\frac{T_2}{T_{wg}}\right| = \frac{1}{\sqrt{1+\omega^2 G_2^{-2} C_2^2}}, \tag{2.8a}$$

$$\left|\frac{T_1}{T_2}\right| = \frac{1}{\sqrt{1+\omega^2 G_1^{-2} C_1^2}}, \tag{2.8b}$$

$$\left|\frac{T_1}{T_{wg}}\right| = \left|\frac{T_2}{T_{wg}}\right|\left|\frac{T_1}{T_2}\right| = \frac{1}{\sqrt{1+\omega^2 G_1^{-2} C_1^2}}\frac{1}{\sqrt{1+\omega^2 G_2^{-2} C_2^2}}. \tag{2.8c}$$

Here $1/G_1^{-1}$ represents R_1 from Fig. 2.6, $C_1 = \rho V_1 c_v$, and T_{wg} is the temperature of the waveguide body. $\rho = 8920$ kg/m^3 is the density of copper, V_1 is the volume of the copper block labelled "1", and $c_v = 8.0 \times 10^{-3} T$ JK^{-1}kg^{-1} is the specific heat per unit mass of copper valid for the temperatures exploited in these experiments [20]. There are two time constants that need to be calculated, namely, $\tau_1 = \rho V_1 c_v G_1^{-1}$ and $\tau_2 =$

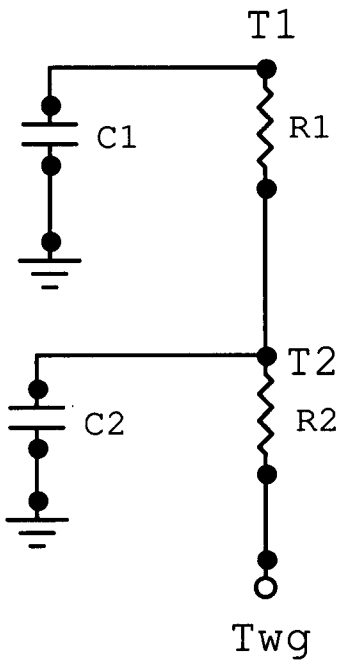

Figure 2.6: Equivalent circuit representation of one of the copper/vespel low-pass thermal filters connecting a thermal stage to the waveguide body.

$\rho V_2 c_v G_2^{-1}$. Before estimating these quantities a value for the thermal conductivity of vespel SP-22 is needed. In 1976, Locatelli *et al.* performed this measurement and report $\kappa_{VP} = (0.0017\ T^2)\ \mathrm{Wm^{-1}K^{-1}}$ valid over the temperature range of 50 mK to 2 K [21]. Provided $T_1 \approx T_2$ Eq 2.6 becomes $G \approx (A/l)\kappa(\bar{T})$, where $\bar{T}$ is the average temperature $(T_1 + T_2)/2$. Given that the outer diameter of the vespel tube is 0.1795 in. and the inner diameter is 0.0995 in. , $A_1 = A_2 = 1.13 \times 10^{-5}\ \mathrm{m}^2$. The lengths of the sections of vespel are $l_1 = 0.131$ in. and $l_2 = 0.263$ in. and the copper blocks have volumes $V_1 = 9.77 \times 10^{-7}\ \mathrm{m}^3$ and $V_2 = 5.42 \times 10^{-7}\ \mathrm{m}^3$, thus at $T = 1.2$ K the two time constants are $\tau_1 = 8.4$ s and $\tau_2 = 9.3$ s. If the modulation frequency is 1 Hz then $|T_1/T_{wg}|$ can be approximated by $\left(\omega^2 G_1^{-1} G_2^{-1} C_1 C_2\right)^{-1}$ resulting in a 3×10^3 suppression of a 1 Hz temperature fluctuation of the waveguide temperature at the sample stage.

2.5 Software

The experiment is controlled and the data recorded using software written using Labview 6.0.2. The program is able to set and control the HP83630A microwave source and two SR850 lock-in amplifiers, one for the reference stage and one for the sample stage, and write and save the necessary data into a file. The user enters the start frequency, end frequency, and the frequency step size of the desired sweep. The program will then step through all the frequencies recording the current frequency,

the sample Cernox voltage signal, the reference Cernox voltage signal, the ratio of the sample and reference signals, and the microwave power. At each frequency the lock-in detectors sample the Cernox voltages for a period of about 60-80 seconds, after which all of the data that has been sampled is averaged. This average result is then recorded to the data file.

The software can be run in either of two modes. In "constant power" mode, the microwave power *of the synthesizer* is set by the user at the beginning of the frequency scan and is left constant throughout the entire scan (because of standing waves in the microwave circuit the magnetic field H_{rf} at the sample site is *not* constant, see below). In the second mode the user supplies the program with a desired sample signal level and a tolerance. The program then uses this signal level and tolerance to set the microwave power for each frequency in the scan. To accomplish this at each frequency the software takes a snapshot reading of the Cernox voltage and compares it to the desired signal level. If the reading is outside the acceptable tolerance the program calculates the change in microwave power needed to correct signal level. After changing the power another snapshot is taken to ensure that the signal level is now correct and then the program begins sampling the Cernox voltage. The advantage of running in the first mode is that the time needed to complete an entire scan is much shorter. In the second mode, each time the power is changed the program waits a settling time (typically 60 seconds) before continuing. Thus the same scan done in the constant power mode can finish in approximately half the time needed to run the constant signal level mode. The advantage of the constant signal level mode is that the user is assured that the signal level gets neither too small nor too large. Because of the complex microwave circuit in the experiment, microwaves are coupled into the rectangular coaxial structure more or less efficiently at different frequencies. This means that at a fixed microwave power the signal levels at two separate frequencies can differ significantly. If the signal level becomes much lower than the sensitivity setting on the lock-in detector the signal to noise ratio of the measurement is compromised, and if the signal becomes too high the thermal stage can be driven nonlinear, in which case the detection method is no longer reliable. Running in the constant signal level mode alleviates both of these concerns.

Chapter 3

Design of Rectangular Coaxial Transmission Line

3.1 Design Considerations

Fig. 3.1 shows (i) the cross-section of a rectangular coaxial line with samples located on either side of the septum, (ii) the electromagnetic field configurations for the TEM mode which propagates at all frequencies, (iii), and (iv) the field configurations for the two TE modes with the lowest cut-off frequencies, namely the TE_{10} and TE_{01} modes. The magnetic field of the TEM mode loops symmetrically around the inner conductor in the plane of the page and its magnitude is identical at each of the sample sites. The TE modes propagate only above their respective cut-off frequencies and the magnetic fields form closed loops that are not restricted to the plane of the page. Notice that the fields from either of the TE modes add anti-symmetrically to the TEM mode fields so that the total magnetic fields at the two sample sites are no longer equivalent causing a breakdown of the ratio technique. The TE_{01} mode is particularly damaging because the magnetic field strength at the sample sites is large, whereas the magnetic field from the TE_{10} mode is largely screened from the samples by the broad septum.

When designing the rectangular transmission line for the bolometry experiment there are several design criteria that must be kept in mind.

1. The impedance of the coaxial line should be matched to that of the cylindrical coaxial cable ($z_o = 50\ \Omega$) used to deliver microwaves to the experiment, this ensures maximum microwave power transfer into the waveguide structure.

2. The septum should be broad (i.e. C large) so that the microwave fields are as uniform as possible over the surface of the samples. Typical sample dimensions are 1 mm×1 mm.

3. The distance $(B - D)/2$ should be large enough to allow ample clearance for sample loading.

4. Dimensions need to be selected to ensure that the cut-off frequencies of the symmetry breaking TE_{01} and TE_{10} modes are as high as possible, while maintaining criteria (1), (2), and (3).

5. There is a geometrical discontinuity at the connection between the cylindrical coaxial cable and the rectangular transmission line. Despite impedance matching, this discontinuity can result in reflections of microwaves signals resulting

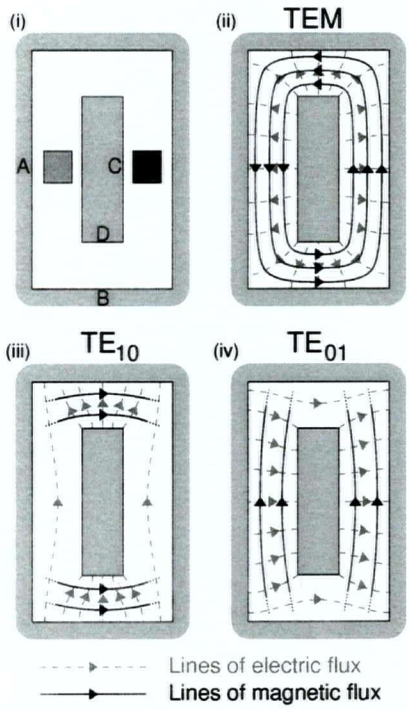

Figure 3.1: (i) Schematic of the cross-section of a rectangular coaxial line. Samples are positioned symmetrically on the two sides of the broad inner conductor. (ii) Field configuration for the TEM mode. The magnetic field loops around the inner conductor in the plane of the page. The magnitude of the magnetic field is identical at the two sample sites. (iii) and (iv) Field configurations for the TE_{10} and TE_{01} modes respectively. For these modes the fields are not restricted to the plane of the page. Notice that when either of the TE_{10} or TE_{01} modes are added to the TEM mode the field strengths at the two sample sites differ causing a breakdown of the ratio technique. A, B, C, and D denote the dimensions of the line segment to which they are closest.

in resonances within the waveguide structure. Making the length of the septum relatively short will raise the resonance frequencies of the TE_{01} and TE_{10} modes.

Consideration (5) is important because the TE_{01} and TE_{10} modes may not be present immediately above their cut-off frequencies if the rectangular transmission line is very symmetric; in fact it has been observed that these modes can be shifted to somewhat higher frequencies.

In his book Gunston [22] gives an expression for the impedance of a rectangular coaxial line that was first worked out by Bräckelmann:

$$z_o\sqrt{\kappa} = 59.952 \ln\left(\frac{A+B}{C+D}\right), \tag{3.1}$$

where κ is the relative dielectric constant of the medium between the conductors. This result is stated to be accurate to 10% provided $D/B < 0.3$ and $C/A < 0.8$. Both of these inequalities are satisfied for the current design.

To calculate the cut-off frequencies the work of Pyle [23] is followed. In his paper Pyle outlines a method for calculating the cut-off frequency for the TE_{10} mode in a ridged waveguide of any aspect ratio to within a few percent. His technique involves representing the TE_{10} mode inside the waveguide as two converging TEM waves. Solving for the wavelength λ that requires that the two TEM wave fronts are parallel is equivalent to solving for the TE_{10} cut-off wavelength λ_c. Fig 3.2 shows how the TE_{01} and TE_{10} modes of a rectangular transmission line can be mapped onto the TE_{10} mode of a ridged waveguide by strategically inserting conducting walls that do not alter the field configuration in the rectangular transmission line. Applying

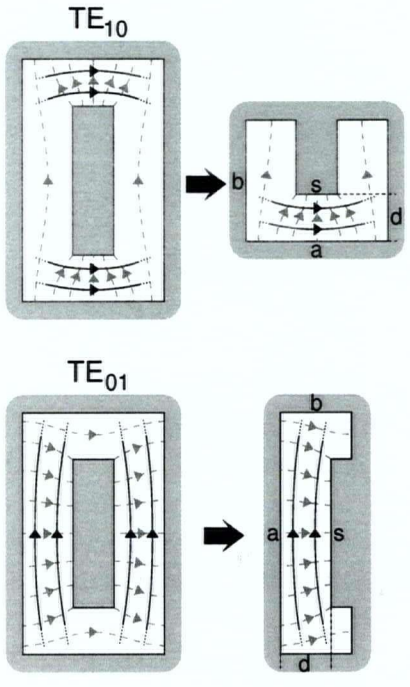

Figure 3.2: Top: Placing an imaginary horizontal conducting wall halfway up the rectangular coaxial line maps the electromagnetic fields of the TE_{10} mode onto fields of the TE_{10} mode of a ridged waveguide. The conversions to the labels of Fig. 3.1(i) are $A = 2b$, $B = a$, $C = 2(b-d)$, and $D = s$. Bottom: Placing an imaginary vertical conducting wall centred on the rectangular coaxial line maps the electromagnetic fields of the TE_{01} mode onto fields of the TE_{10} mode of a ridged waveguide. Here $A = a$, $B = 2b$, $C = s$, and $D = 2(b-d)$.

Pyle's method for calculating cut-off frequencies of a rectangular coaxial line is valid provided the septum is not too thin (i.e. provided D is not $\ll (B-D)$).

Mode	Cut-off (GHz)	$\frac{1}{4}$-wave (GHz)	$\frac{1}{2}$-wave (GHz)
TE_{01}	3.84	4.78	6.86
TE_{10}	4.93	5.69	7.52

Table 3.1: Cut-off frequencies and 1/4 and 1/2-wave resonances of the TE_{01} and TE_{10} modes for the ×4 scale model.

The waveguide dispersion relation is given by:

$$\omega = \sqrt{\omega_c^2 + c^2k^2}, \tag{3.2}$$

where ω_c is the cut-off frequency for a particular mode, k is the wave number, and c is the speed of light. As discussed earlier in the section, the geometric discontinuity between the cylindrical and rectangular transmission lines can cause reflections of the microwave signals which will allow for resonances within the waveguide structure. Quarter-wave and half-wave resonance frequencies can be evaluated by allowing k to take on values that correspond to a quarter and a half of a wavelength λ fitting inside the length L of the rectangular transmission line. These values are $k = \pi/(2L)$ and $k = \pi/L$ respectively ($k = 2\pi/\lambda$). Substituting these k values into Eq 3.2 yields:

$$\omega_{\frac{1}{4}} = \sqrt{\omega_c^2 + \frac{c^2\pi^2}{4L^2}}, \tag{3.3a}$$

$$\omega_{\frac{1}{2}} = \sqrt{\omega_c^2 + \frac{c^2\pi^2}{L^2}}, \tag{3.3b}$$

where $\omega_{\frac{1}{4}}$ and $\omega_{\frac{1}{2}}$ are the quarter and half wave resonances respectively. The quarter-wave resonance corresponds to an open circuit termination (electric field anti-node) of the septum where the connection to the circular coaxial cable is made, while the half-wave resonance corresponds to a short circuit termination (electric field node). The short circuit termination is preferred because its resonance frequency is higher than that of the open circuit case. To encourage short circuit termination a high capacitance region is desired where the connection of the septum to the cylindrical coaxial cable is made.

3.2 Test of a ×4 Scale Model

An Agilent 8510C Vector Network Analyzer (VNA) was used to test a ×4 scale model of the first generation bolometry experiment developed by Patrick Turner. The dimensions of the model are as follows: $A = 35.6$, $B = 16.2$, $C = 19.8$, $D = 3.6$, and $L = 26.4$ mm. Table 3.1 summarizes the cut-off frequencies and 1/4- and 1/2-wave resonances for the TE_{01} and TE_{10} modes for the scale model. A digital photo of the scale model is shown in Fig 3.3. The inner conductor of the cylindrical coaxial

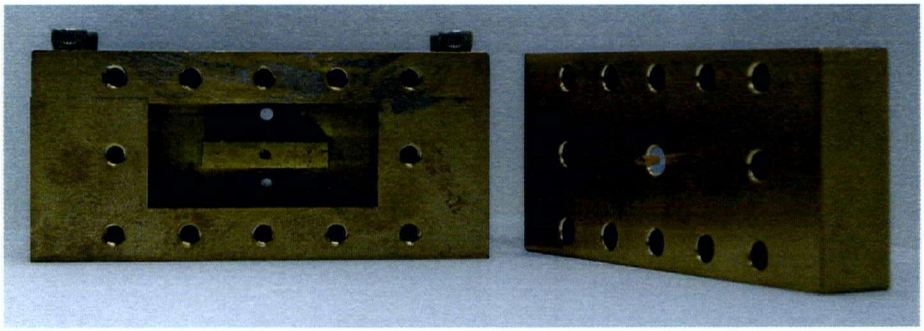

Figure 3.3: $\times 4$ scale model of the rectangular coaxial structure used by Patrick Turner

cable is inserted into a small centred hole drilled in the septum along with a small piece of indium wire to ensure good electrical contact. This assembly technique promotes a high capacitance region between the inner and outer conductors of the rectangular transmission line where the connection to the cylindrical coaxial cable is made and is similar to the design used for the experiment built during this thesis. This capacitance should be thought of as a shunt capacitance from the septum to ground. If this capacitance is sufficiently large it behaves as a direct path to ground and favours short circuit termination. The VNA has a frequency range from 45 MHz to 50 GHz and is used as the microwave source as well as the detector, capable of measuring both amplitude and phase. To detect the microwaves a small coupling loop, made by shorting the inner conductor of a standard .085 in. coaxial cable to its outer conductor, was used (see Fig 3.4). This coupling loop was inserted into the

Figure 3.4: Coupling loop used to detect microwaves inside the waveguide body.

waveguide such that the loop was positioned at a sample site. Amplitude data was taken first on one side of the septum and then at an equivalent site on the opposite side of the septum. One would expect that up to the lowest TE mode cut-off frequency the two sets of amplitude data should ratio to one. However, as mentioned above, these modes may not be excited until somewhat higher frequencies if the geometry of the rectangular transmission line is very symmetric.

Fig 3.5 shows the amplitude of the ratio of the two data sets over a frequency range of 50 MHz to 10 GHz. The ratio is very close to one up to a frequency of ≈

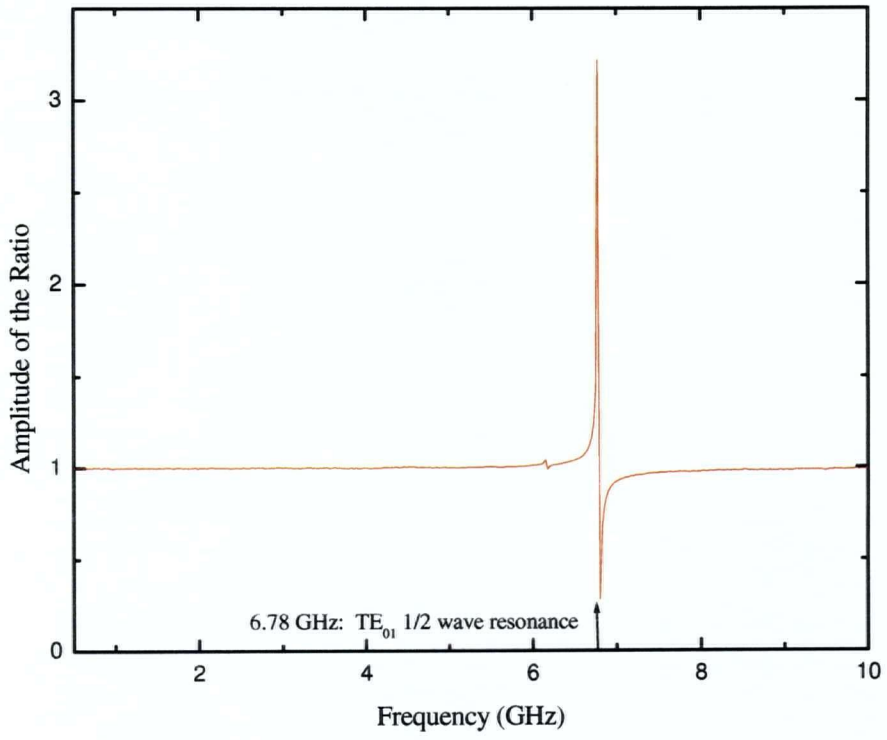

Figure 3.5: Plot of the Amplitude of the ration verse frequency. The first departure from a ratio of one is observed at the 1/2-wave resonance of the TE_{01} mode.

6.78 Ghz, which exceeds the cut-off frequencies for both the TE_{10} and TE_{01} modes. The first departure from a ratio of one corresponds to the 1/2-wave resonance of the TE_{01} mode indicating the high capacitance region between the septum and waveguide body.

3.3 Performance of the Final Design

The final dimensions of the rectangular coaxial structure built during this thesis are $A = 5.64$, $B = 3.76$, $C = 3.25$, $D = 0.76$, and $L = 6.63$ mm. Using these dimensions and Eq. 3.1 results in an impedance of $z_o = 51.1\ \Omega$. Table 3.2 summarizes the results of the TE mode calculations.

In order for this experiment to produce meaningful results it is imperative to demonstrate that the ratio technique described in §2.3 works over a broad frequency range. This requirement is best tested by placing identical metal samples on both the reference and sample thermal stages. Then, as can be seen from Eq. 2.4, the ratio of

Mode	Cut-off (GHz)	$\frac{1}{4}$-wave (GHz)	$\frac{1}{2}$-wave (GHz)
TE_{01}	24.47	26.96	33.33
TE_{10}	24.37	26.89	33.25

Table 3.2: Cut-off frequencies and 1/4 and 1/2-wave resonances of the TE_{01} and TE_{10} modes for the dimensions given in the text.

the two powers is just equal to the ratio of the surface area of the samples, that is:

$$\frac{P^{sam}}{P^{ref}} \frac{A^{ref}}{A^{sam}} = 1. \tag{3.4}$$

It is unlikely that the ratio above will actually be one, since any asymmetries in the construction of the rectangular coaxial structure may cause the field H to differ on opposite sides of the inner conductor. This effect is not a major concern provided that the ratio is *constant* across the desired frequency range. Once numerical value of the above ratio is known, subsequent data can be corrected for this systematic affect. Fig. 3.6 shows detailed ratio data from 0.2 to 24.0 GHz taken with two Ag:Au metal samples in place. The ratio is flat to within 3% over this frequency range with

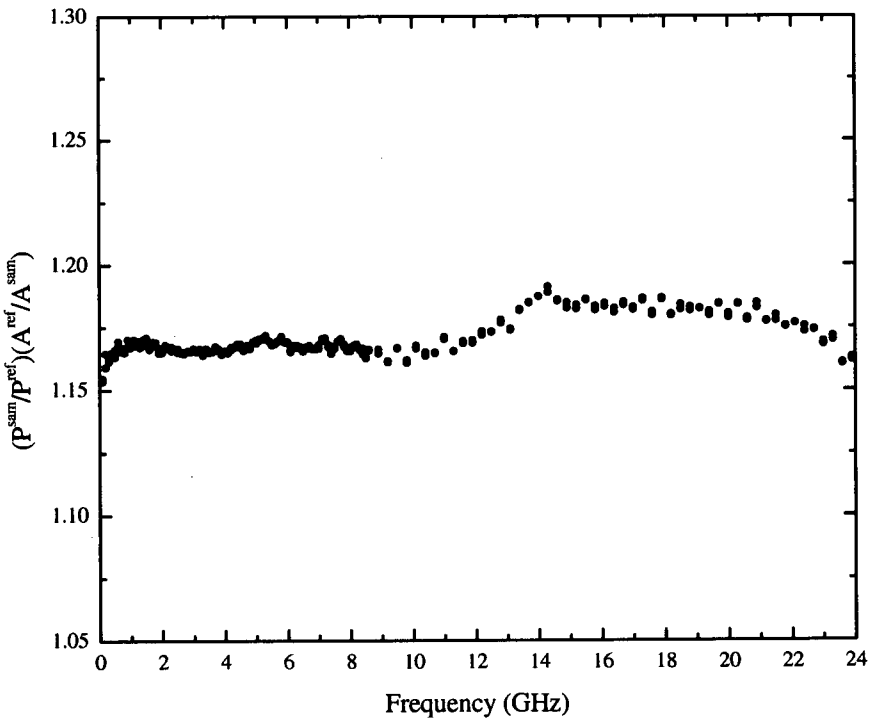

Figure 3.6: Ratio of data taken using two Ag:Au metal samples. The ratio is flat to 3% and has an average value of 1.17.

an average value of 1.17. A slight twist of the inner conductor with respect to the outer conductor is thought to have caused the ratio to differ from one. The twist was measured to be 1.9°.

A high frequency scan is shown in Fig. 3.7 showing where the ratio technique fails due to the onset of symmetry breaking TE modes. The first departure from a ratio

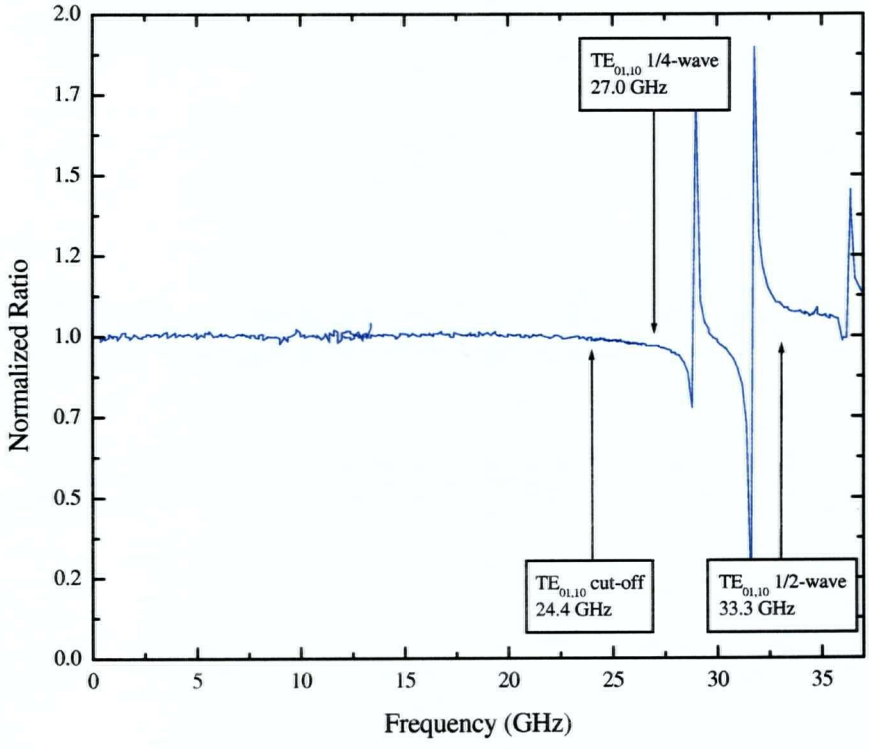

Figure 3.7: 0-37 GHz plot of normal metal ratio. The $TE_{01,10}$ cut-off and 1/4- and 1/2-wave resonance frequencies have been indicated.

of one is seen to occur soon after the 1/4-wave resonance of the TE modes. It is unfortunate that, despite efforts to promote short circuit termination, the flat ratio did not persist to the higher 1/2-wave resonance. Again it is suspected that the twist of the septum is the problem, causing a premature onset of the TE modes.

Chapter 4

Experiment Performance and Evaluation

Although the experiment built was ultimately designed to be used in a ^{3}He/^{4}He dilution refrigerator and operated at $\sim$ 100 mK, a testing phase was first performed at 1.2 K using a pumped liquid ^{4}He bath. All the measurements reported in this chapter were part of this testing phase.

4.1 Sensitivity and Thermal Conductance

The conductances of the thermal weak links for both the reference and sample stages were measured at several temperatures and compared to the design values. The thermal conductance of a material of cross-sectional area, A, and length, l, is defined as the ratio of input power to the temperature difference across the material: $G = P/\Delta T$. From the discussion at the end of §2.3, the power is given by a calibration factor β multiplied by the change in voltage across the Cernox sensor, so:

$$G = \beta \frac{\Delta V}{\Delta T} A_v = \beta \frac{\Delta V}{(\mathrm{d}T/\mathrm{d}R)\,\Delta R} A_v = \beta I_B \left.\frac{\mathrm{d}R}{\mathrm{d}T}\right|_{T=T_B} A_v. \tag{4.1}$$

An additional factor A_v has been inserted because the signal from the Cernox sensor is amplified before reaching the lock-in detector. A_v is the gain of the amplifier and must be included in Eq. 4.1. Fig. 4.1 is a plot of the resistance of one of the Cernox1050 sensors verses temperature derived from the vapour pressure of the liquid ^{4}He in the dewar. These data are used to calculate $\mathrm{d}R/\mathrm{d}T$. The thermal conductance measurements were performed at 1 Hz and at this frequency the amplifier has a gain $A_v = 9735$. Once the thermal conductance has been measured, the thermal conductivity is easily determined using $\kappa\left(\bar{T}\right) = (l/A)\,G\left(T\right)$.

The quartz tube that serves as the thermal weak link for the sample stage has a cross-sectional area of $A = 0.814$ mm^2 and a length of $l = 12.3$ mm. Table 4.1 summarizes the results of the thermal conductance measurements of this quartz tube. R. B. Stephens reports that the thermal conductivity of quartz for temperatures below $\sim$ 1 K is given by $2.4 \times 10^{-2} T^{1.87}$ Wm^{-1}K^{-1} [24]. Fig. 4.2 compares this reported value with the data from Table 4.1 and one sees good agreement at the two lower temperatures. Stephens' expression is not valid above 1 K and so the discrepancy at 10 K is not surprising.

These measurements were also performed for the stainless steel tube used as the thermal weak link for the reference stage. The stainless steel tube has a cross-sectional

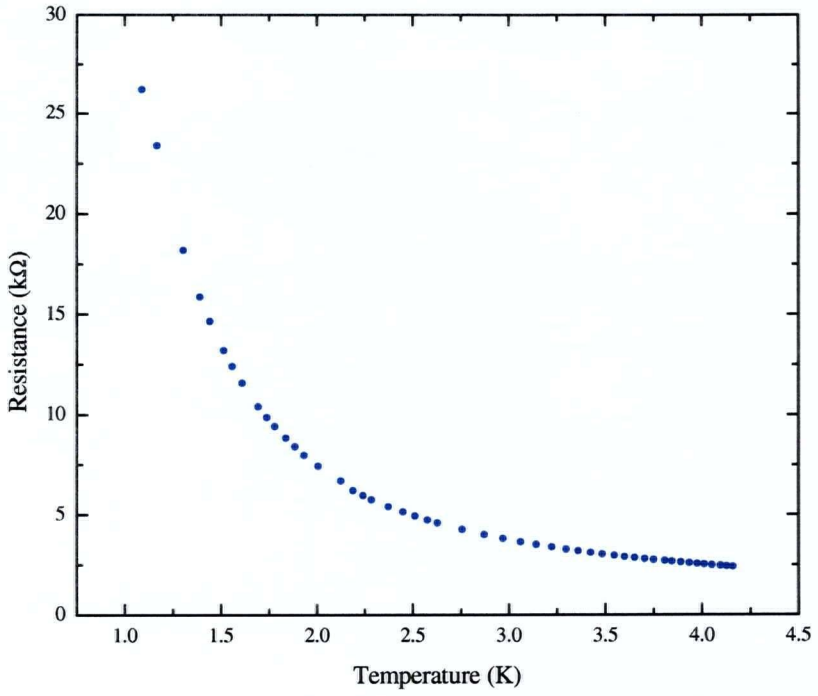

Figure 4.1: Low temperature calibration of the Cernox 1050 bolometer via ^{4}He vapour pressure thermometry.

T_B (K)	I_B (μA)	$\frac{dR}{dT}\big\vert_{T=T_B}$ $\left(\frac{k\Omega}{K}\right)$	cal $\left(\frac{nW}{V}\right)$	G $\left(\frac{\mu W}{m \cdot K}\right)$	κ $\left(\frac{W}{K}\right)$
1.25	1.52	33.55	4.41	2.190	0.0331
2.52	28.29	2.99	10.45	8.613	0.130
9.97	257.5	.081	755.2	154.3	2.332

Table 4.1: Thermal conductivity data for the sample stage quartz tube.

area of 0.48 mm^2 and is 2.54 mm long. The measured thermal conductivity did not behave in the expected manner; at low temperatures the measured thermal conductivity was smaller than expected, moreover the data did not extrapolate to $\kappa(T \rightarrow 0) = 0$ in the expected linear manner. An explanation for this strange behaviour cannot be provided at the time of this writing, but a plausible cause is offered. The sapphire plate that supports the bolometer, heater, and sample is glued into the end of the stainless steel tube using Stycast 1266 epoxy. The thermal conductance of the epoxy has been estimated and it was found to be comparable to that of the stainless steel tube at low temperature ($\sim$ 1 K). Since these thermal conductances act in series with each other, the excess thermal conductance of the glue could account for the low conductivity values measured at the low temperatures. A new reference thermal stage is currently under construction in which the end of the tube has been pinched flat so

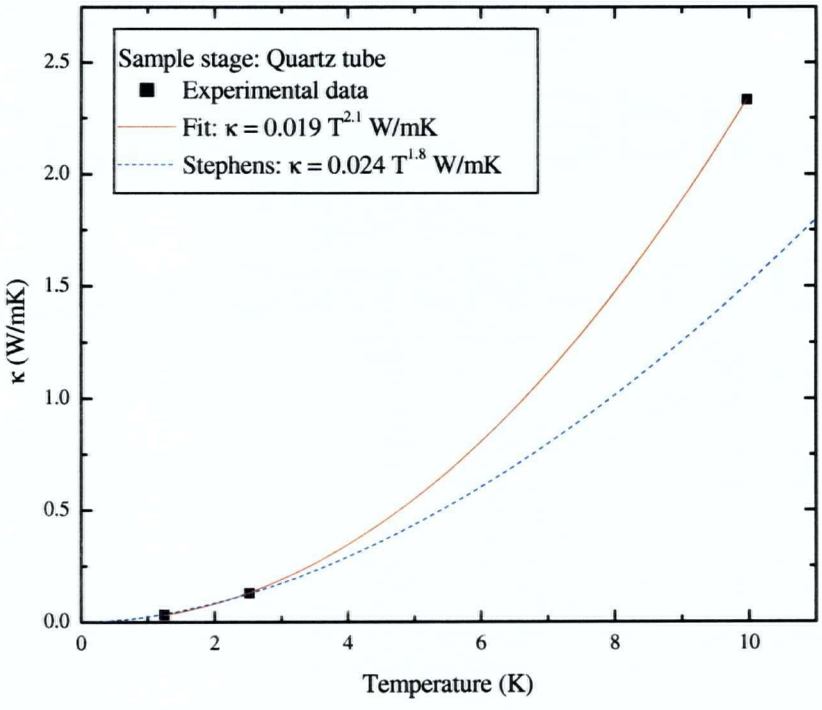

Figure 4.2: Thermal conductivity of the sample stage quartz tube as a function of temperature.

that much less epoxy will be required to hold the sapphire plate in place resulting in an increased thermal conductance between the sapphire and stainless steel.

4.2 Frequency Response of Thermal Stages

Because the microwave field in the coaxial structure is modulated at a low frequency (1 Hz - 5 Hz) it is important to ensure that the corner frequencies of the thermal stages be comparable or above this modulation frequency in order avoid losing valuable signal. At the same time it is beneficial to operate at as high a modulation frequency as possible in order to reduce the effects of $1/f$ noise, which is always present. In this experiment one could have $1/f$ type fluctuations in the base temperature, and $1/f$ electrical noise in both the bolometer and the amplifier. We wish to calculate temperature response of the thermal stage to a sinusoidal input power, $\dot{Q}$ (see Fig 2.3). It is assumed that the isothermal sample stage (sapphire plate, sample, thermometer, and heater) has a negligible thermal mass and is connected to a base temperature, T_o via a weak thermal link with a distributed heat capacity c_v per unit volume. Assuming that the AC heat input takes the form $\dot{Q} = \dot{Q}_1 e^{i\omega t}$, the steady state temperature response becomes $T = T_1 e^{i\omega t}$. In this analysis it will be useful to define the thermal diffusivity, $\alpha = \kappa/c_v$, which has dimensions of m^2/s. Here, the aim is to calculate the coefficient T_1 at the sample site, which will be denoted $T_1(x = 0) = T_\omega$. Substituting

this relation into the one-dimensional heat equation:

$$\frac{\partial T}{\partial t} = \alpha \frac{\partial^2 T}{\partial x^2}, \tag{4.2}$$

yields:

$$\mathrm{i}\omega T_1 = \alpha \frac{\partial^2 T_1}{\partial x^2}, \tag{4.3}$$

with the boundary conditions:

$$x = 0 \rightarrow T_1 = T_\omega, \tag{4.4a}$$
$$x = l \rightarrow T_1 = 0. \tag{4.4b}$$

Subject to these boundary conditions Eq. 4.3 has the following solution:

$$T_1 = T_\omega \sinh\left[\frac{1+\mathrm{i}}{\delta}x\right]\left(\coth\left[\frac{1+\mathrm{i}}{\delta}x\right] - \coth\left[\frac{1+\mathrm{i}}{\delta}l\right]\right), \tag{4.5}$$

where the thermal penetration depth has been defined as $\delta = \sqrt{2\alpha/\omega}$. Applying conservation of energy requires $\dot{Q} = -\kappa A(\partial T/\partial x)_{x=0}$, or:

$$\dot{Q}_1 = -\kappa A\left(\frac{\partial T_1}{\partial x}\right)_{x=0}. \tag{4.6}$$

Combining Eq 4.5 with Eq 4.6 leads to:

$$|T_\omega| = \frac{\dot{Q}_1}{G}\frac{l_{eff}}{l}, \tag{4.7}$$

where an effective length has been defined as:

$$l_{eff} = \frac{\delta}{\sqrt{2}}\left(\frac{\cosh\left[2\frac{l}{\delta}\right] - \cos\left[2\frac{l}{\delta}\right]}{\cosh\left[2\frac{l}{\delta}\right] + \cos\left[2\frac{l}{\delta}\right]}\right)^{\frac{1}{2}}. \tag{4.8}$$

A more transparent form for l_{eff} can be obtained by expanding the trigonometric functions in a Taylor series keeping the first three non-zero terms:

$$l_{eff} = l\left[\frac{1}{1+\omega^2\left(\frac{l^4}{6\alpha^2}\right)}\right]^{\frac{1}{2}}, \tag{4.9}$$

	sample	reference
κ ($\times 10^{-2}$Js^{-1}m^{-1}K^{-1})	3.6	17.6
c_v (Jm^{-3}K^{-1})	13.8	1225
α ($\times 10^{-4}$m^{2}s^{-1})	26.1	1.4
l ($\times 10^{-3}$m)	12.1	2.6
f_o (Hz)	6.9	8.3

Table 4.2: Summary of the calculated corner frequencies f_o and the parameters used for the sample and reference thermal stages at $T = 1.25$ K.

which, when substituted into Eq 4.7 allows one to write $|T_\omega|$ in a form reminiscent of a single pole low pass filter:

$$|T_\omega| = \frac{\dot{Q}_1}{G}\left[\frac{1}{1+\omega^2\left(\frac{l^4}{6\alpha^2}\right)}\right]^{\frac{1}{2}}, \tag{4.10}$$

giving a corner frequency $\omega_o = \sqrt{6}\alpha/l^2$. Again we refer to the work of Stephens to obtain the low temperature specific heat of quartz glass which he reports to be $c_v = 2.9$ Jkg^{-1}K$^{-2}T + 5.2$ Jkg^{-1}K$^{-4}T^3$ [24]. Table 4.2 summarizes the relevant quantities for both the sample and reference thermal stages at a temperature of 1.25 K. The frequency response of the thermal stages was measured by passing an AC current through the chip heater and measuring the response of the bolometer at frequency ω. The peak AC current remained constant and only ω was varied. Fig. 4.3 shows the measured frequency response of the sample stage. The blue line represents the curve for a single pole loss pass filter of Eq. 4.10 with a corner frequency of 4 Hz and the red curve was generated using Eqs. 4.7 and 4.8 from the full distributed heat capacity analysis. The measured corner frequency of 4 Hz falls short of the expected 6.9 Hz and may be the result of a combination of factors. The corner frequency depends quite strongly on the length l which is not precisely defined because of the method of construction. If the actual length of the tube is somewhat longer than the measured value, then the corner frequency will certainly drop. In fact the red curve shown in Fig. 4.3 was generated using $l = 16$ mm (note that $l = 16$ mm also will give $f_o \approx 4$ Hz in the single pole filter analysis). Also, the analysis presented above ignores the combined lumped heat capacities of the sapphire plate, chip heater, and bolometer. Taking this extra heat capacity into account will reduce the corner frequency, although its effect is *expected* to be negligible.

Again the results obtained for the reference stage showed very unusual behaviour. Fig. 4.4 is a plot of the measured frequency response of the stainless steel reference stage. These unexpected findings are thought to be caused by the excess epoxy. Not only does the epoxy alter the effective thermal conductance, it also introduces a large lumped heat capacity at the end of the stainless steel tube. This additional heat capacity will certainly alter the frequency response of the reference stage. The new

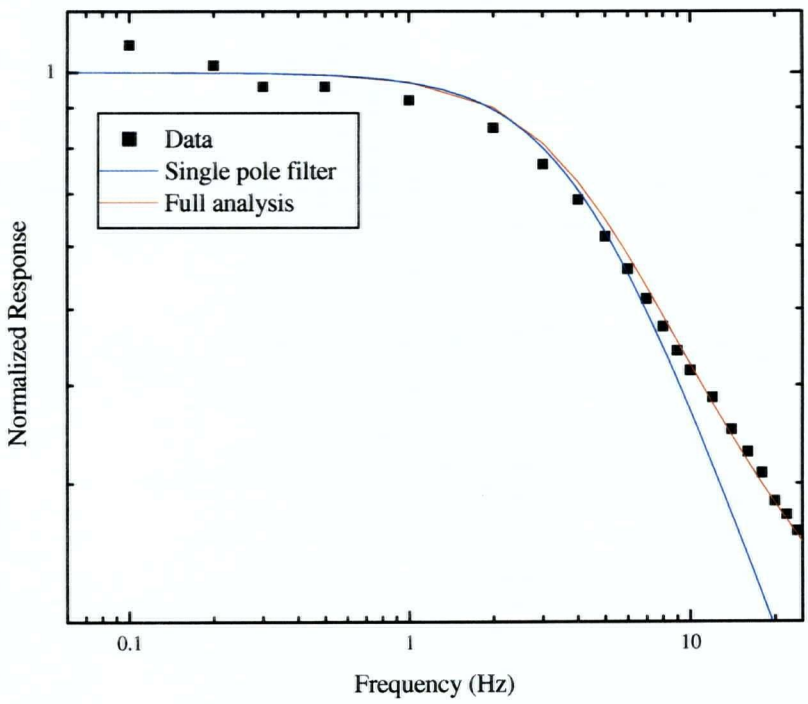

Figure 4.3: Frequency response of the quartz tube sample stage. The blue line is for a single pole low-pass filter and the red line takes into account the distributed heat capacity of the quartz tube.

design discussed at the end of the previous section is expected to remedy the unusual behaviour that has been observed.

4.3 Minimum Detectable Power

In this section an expression for the minimum detectable power of the bolometer sample stage is calculated. The sample stage is heated to its operating temperature by passing a bias current I_B through the bolometer whose resistance is R_B. When microwave power P_s is absorbed by the sample the temperature of the isothermal sapphire stage is raised. This temperature rise is detected as a change in voltage δV_B of the bolometer and is given by:

$$\delta V_B = I_B \left(\frac{\mathrm{d}R_B}{\mathrm{d}T} \right) \delta T_B. \tag{4.11}$$

The change in temperature is determined by the thermal conductance G of the thermal weak link connecting the sample stage to base temperature T_o, that is $\delta T_B = P_s/G$. In terms of the dimensionless sensitivity of the bolometer, defined

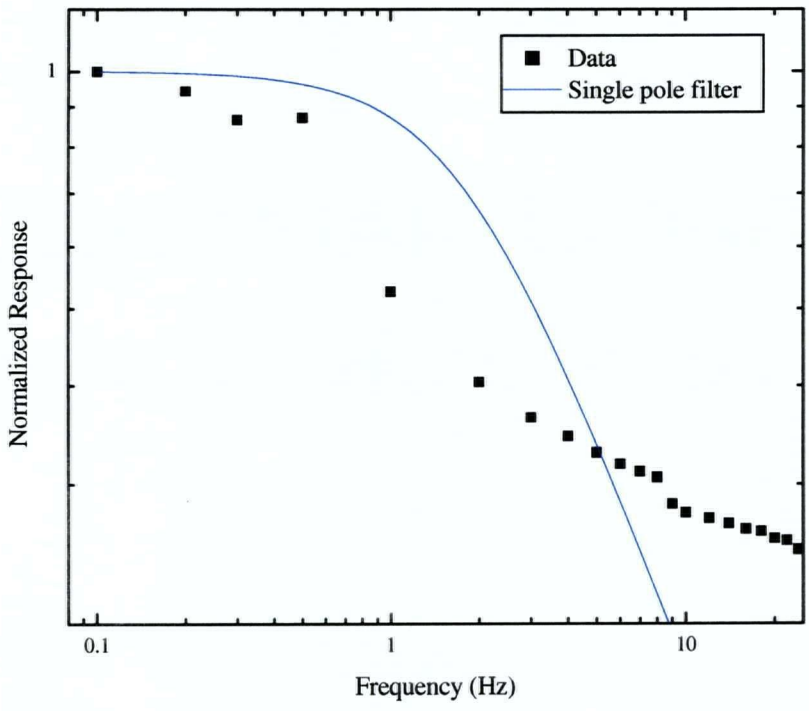

Figure 4.4: Plot of the unusual frequency response observed for the stainless steel tube of the reference stage. The blue line is a fit to a single pole low-pass filter with a corner frequency of $f_o = 1.8$ Hz.

as:

$$S_d = \frac{\mathrm{d}\left(\log R_B\right)}{\mathrm{d}\left(\log T_B\right)} = \frac{T_B}{R_B}\left|\frac{\mathrm{d}R_B}{\mathrm{d}T_B}\right|, \tag{4.12}$$

Eq 4.11 becomes:

$$\delta V_B = I_B \frac{R_B}{T_B} S_d \frac{P_s}{G}. \tag{4.13}$$

The thermal conductance, G, can be written in terms of the temperature difference across the thermal weak link and the power ($I_B^2 R_B$) delivered to the bolometer: $G = P_B/\left(T_B - T_o\right)$, so:

$$\delta V_B = I_B R_B \frac{T_B - T_o}{T_B} S_d \frac{P_s}{P_B}. \tag{4.14}$$

Next, a threshold detectable signal v_n is defined as the thermal noise generated in a frequency bandwidth $\Delta\nu$ in the bolometer:

$$\overline{v_n^2} = 4 k_B T_B R_B \Delta\nu, \tag{4.15}$$

where k_B is Boltzmann's constant. The bandwidth $\Delta\nu$ is determined by the time constant and filter settings of the lock-in amplifier. Typical settings of a 1 s time constant and a 24 dB/octave filter give $\Delta\nu = 78$ mHz. Finally, equating δV_B to the

threshold detectable signal $\left(\overline{v_n^2}\right)^{1/2}$ allows one to write:

$$P_s^{min} = \frac{2}{\gamma S_d}\sqrt{P_n P_B}, \tag{4.16}$$

where $\gamma \equiv (T_B - T_o)/T_B$ and the noise power is $P_n = k_B T_B \Delta\nu$.

Fig. 4.1 shows the low temperature ^{4}He vapour pressure calibration of the Cernox 1050 bolometer. From these data the dimensionless sensitivity of the bolometer at $T_B = 1.25$ K can be calculated to be $S_d = 2.12$. In a typical run the pumped liquid ^{4}He bath achieves a base temperature of $T_o = 1.1$ K and the temperature of the bolometer is set to 1.25 K using a bias current of $I_B = 1.5$ μA. At this temperature the Cernox has a resistance of 20.2 kΩ, thus the power is $P_B = 45.5$ nW. Substituting these numbers into Eq. 4.16 one expects a minimum detectable power of 1.9 fW. In §2.2 the magnetic field H at the sample site was calculated to be 3.7 Am^{-1} at 1 GHz. Using this value for H and Eq. 2.2, $P_s^{min} = 1.9$ fW corresponds to a resolution of 140 pΩ in surface resistance for a typical 1 mm$\times$1 mm platelet sample.

Thermal (or Johnson) noise whose value is given by Eq. 4.15 is a source of white noise intrinsic to all resistors and will always set a lower limit on the minimum detectable power for an experiment such as the one described in this thesis. However, most resistive sensors carrying current have excess noise above the level of the intrinsic thermal noise. Clearly, any excess noise will limit minimum detectable power and should be avoided if at all possible. Turner *et al.* [1] measured the noise of their Cernox 1050 sensor and found an additional 40 dB of excess noise, as a result the experimental minimum detectable power was two orders of magnitude greater than their calculated value. These authors also measured the noise of a Haller-Beeman Neutron Transmutation Doped (NTD) germanium cryogenic thermistor [25] and no excess noise was detected. Haller-Beeman manufactures a NTD thermistor (Type H) that would be suitable for dilution refrigerator temperatures. Using calibration data supplied by Haller-Beeman the dimensionless sensitivity of this bolometer was calculated to be 6.73 at $T_B = 100$ mK. If the dilution fridge operates at a base temperature of 50 mK, then $\gamma = 1/2$ and $P_B = 1.09$ nW, resulting in a minimum detectable power of 6.4 aW (6.4×10^{-18} W) and a surface resistance resolution of 0.5 pW at 1 GHz.

Chapter 5

Heat Transfer in the Fridge Design

The success of the bolometric measurement employed in this thesis requires that the temperatures of the sample and reference thermal stages remain very stable. Temperature fluctuations will cause the sensitivities of the thermal stages to vary and will introduce spurious signals when attempting to measure the temperature rise of the samples due to microwave absorption. Both these effects compromise the ratio technique. For experiments performed at 1.2 K and above, the temperature stability of the pumped ^{4}He bath is sufficient that the thermal filtering provided by the vespel tubes described in §2.4 is adequate. However, low temperature measurements to be performed in the dilution refrigerator will require extra care to achieve the necessary temperature stability. This chapter introduces the design developed to adapt the experiment described thus far for use in a dilution fridge. Then the equivalent circuit model introduced in §2.4 is used to numerically calculate the temperature stability of the thermal stages.

5.1 Thermal Filter Design

Low pass thermal filters have been built for both the sample and reference thermal stages. The thermal filters were constructed out of blocks of copper (large specific heat) and short sections of thin-walled stainless steel tubes (low thermal conductivity). The pieces were assembled using Emerson & Cuming Stycast 2850FT black epoxy. The sample side filter consists of two cascaded low pass filters, whereas the reference side has only one low pass filter, which runs through the centre of the sample filters. Less care has been taken to filter the reference stage because the normal metal sample provides large signals that are easily detected. Also, because the reference signals are large, the sensitivity of the reference stage can be safely compromised by operating the stage at a relatively high temperature (say $\sim$ 250 mK), resulting in less stringent requirements for the absolute temperature stability. Fig. 5.1 is a digital photo of the filters and Fig. 5.2 shows a scale drawing of the assembled filters in cross-section.

The low temperature experiments will be performed using a model DRI-420 SHE cooperation dilution fridge. Fig 5.3 is scale drawing of the experimental set-up.

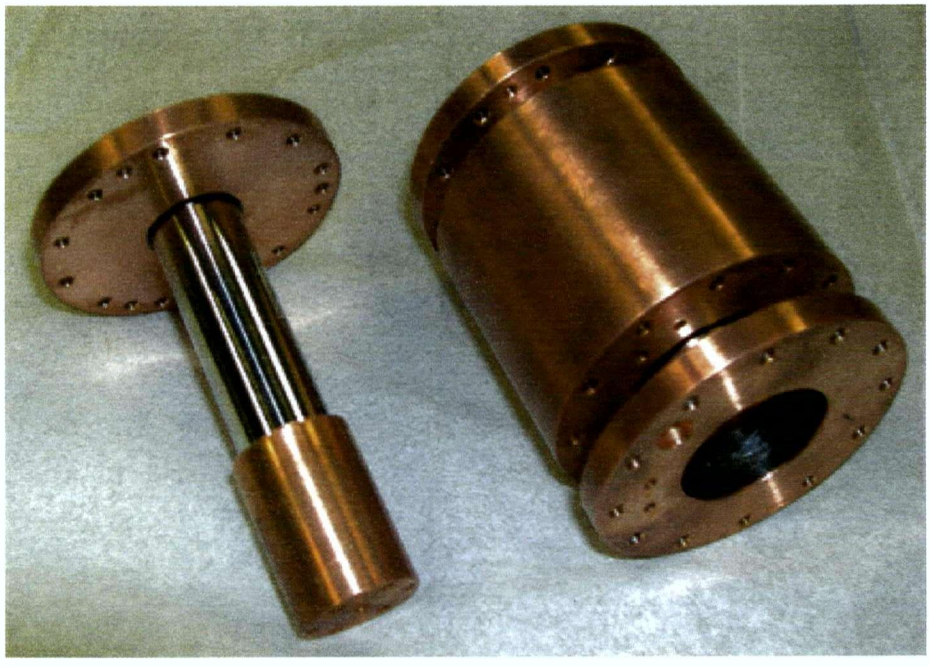

Figure 5.1: Digital photograph of the reference (left) and sample (right) thermal filters.

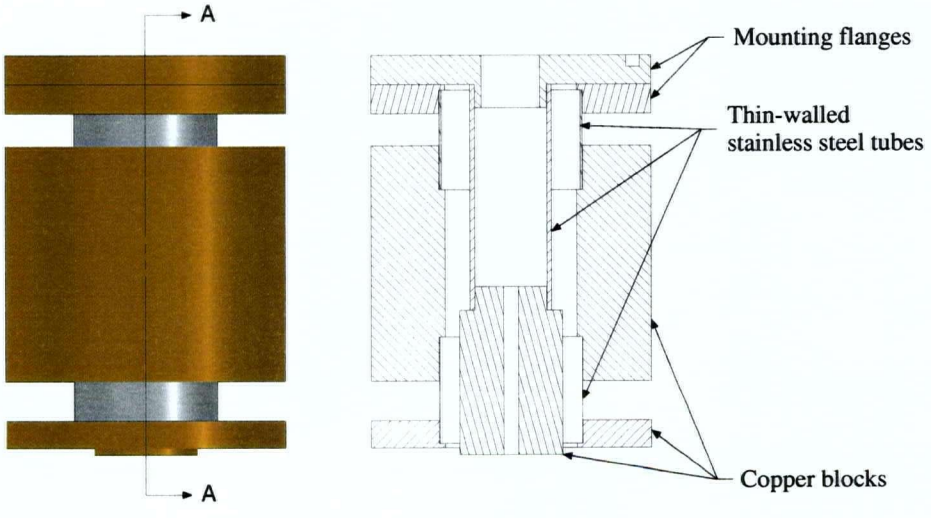

Figure 5.2: Scale drawing of the assembled reference and sample filters including a cross-sectional view.

The main body of the experiment is mounted on the heat shield of the fridge which is thermally and mechanically connected to the still and is at a temperature of $\sim$ 700 mK. The filters hang from the bottom of the mixing chamber which has a base temperature of less than 50 mK. The small copper blocks of the vespel arms are then thermally shorted to the large copper blocks of the filters using 1/16 in. silver wire

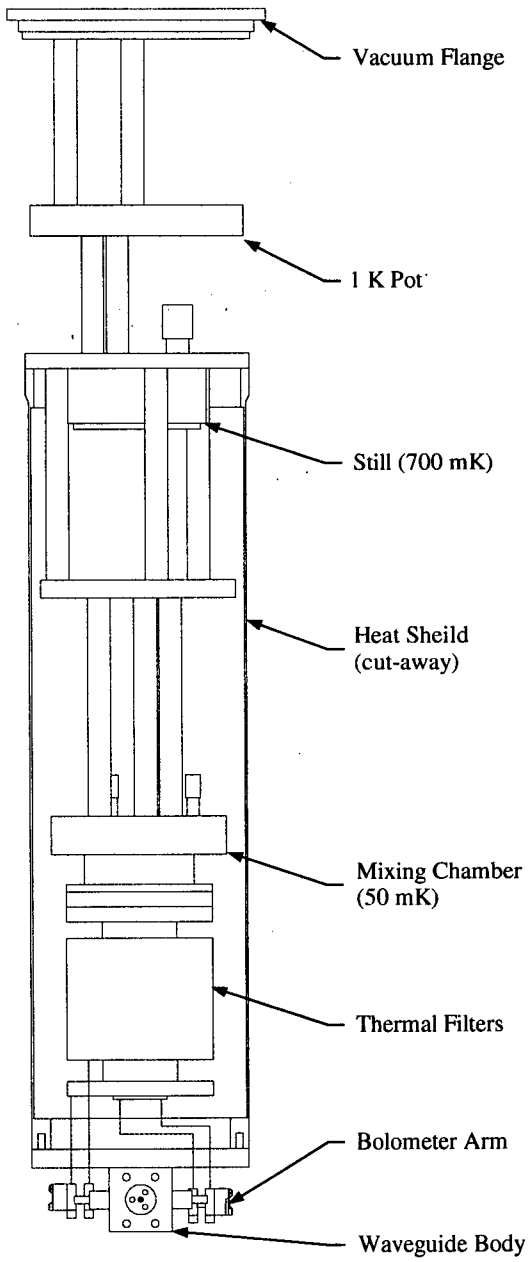

Figure 5.3: Schematic drawing of the bolometry experiment mounted on the dilution fridge. The blue lines represent the silver wires connecting the bolometer arms to the thermal filters.

as shown in the figure. The silver wires pass through small holes drilled through the bottom flange of the heat shield. Fig. 5.4 is a useful cartoon drawing of the set-up shown in Fig. 5.3. The time constants of these filters can be analyzed in exactly the same manner as the vespel filters of §2.4. The volume of the reference copper block is 1.32×10^{-5} m^3 and the stainless steel tube has a cross-sectional area of 5.35×10^{-5} m^2 and a length of 0.0386 m. At a temperature of 50 mK one finds $C_{ref} = 47.1$ μJK^{-1}

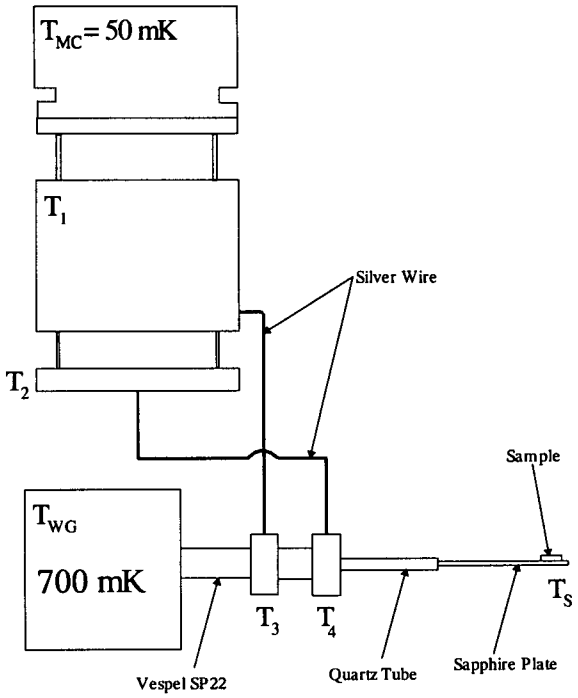

Figure 5.4: Cartoon sketch of the scheme used to connect sample thermal stage to the mixing chamber of the dilution fridge through two cascaded low-pass thermal filters.

and $G_{ref}^{-1} = 1.02 \times 10^5$ KW^{-1}, which gives a time constant of $\tau_{ref} = 4.8$ s and hence a corner frequency of $f_o^{ref} = (2\pi\tau_{ref})^{-1} = 0.03$ rad/s. Note that since $G^{-1} \sim T^{-1}$ and $C \sim T$, τ is temperature independent. As was done for the vespel filters, a good approximation for the suppression of a temperature oscillation at frequency ω is given by the factor $\omega^{-1}\tau_{ref}^{-1}$. The sample filters were designed such that $10G_1^{-1} \approx G_2^{-1}$ and $C_1 \approx 10C_2$ so that $\tau_1 \approx \tau_2$. With volumes of 1.11×10^{-4} m^3 and 1.22×10^{-5} m^3 for the two copper blocks and stainless steel rings with cross-sectional areas of 4.55×10^{-5} m^2 and 4.97×10^{-6} m^2 and lengths of 6.9 mm and 8.9 mm one finds $C_1 = 0.396$ mJK^{-1}, $C_2 = 43.5$ μJK^{-1}, $G_1^{-1} = 21.5 \times 10^3$ KW^{-1}, and $G_2^{-1} = 254 \times 10^3$ KW^{-1}. Thus the relevant time constants are $\tau_1 = 8.5$ s ($\omega_{o1} = .019$ rad/s) and $\tau_2 = 11.1$ s ($\omega_{o2} = .014$ rad/s). Here the suppression of the temperature fluctuations is given by the quantity $\omega^{-2}\tau_1^{-1}\tau_2^{-1}$.

5.2 Cooling the Filters

To test the reliability of the equivalent circuit model that will be used to analyze the filter performance we first use the model to calculate the cooling rate of the filters from liquid N_2 (77 K) to liquid ^{4}He (4.2 K). This calculation will then be compared to data obtained while the filters were actually being cooled in a liquid ^{4}He cryostat. Using the equivalent circuit model developed above leads to the relatively

simple circuit shown in Fig 5.5. In the analysis it is assumed that initially all stages

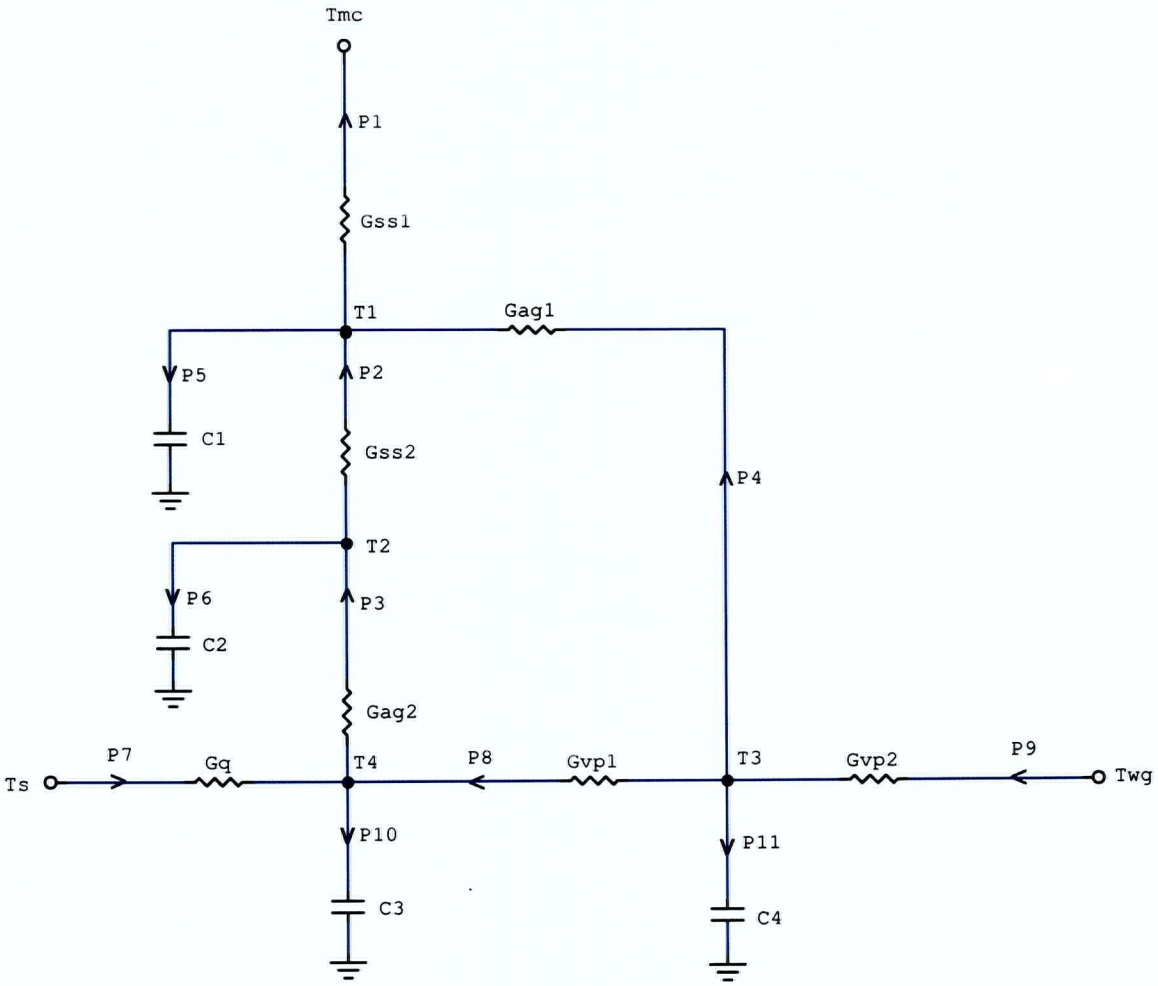

Figure 5.5: Equivalent circuit of the thermal design shown in Fig 5.4.

(T_1, T_2, T_3, and T_4) are in thermal equilibrium at 77 K, then the mixing chamber temperature and waveguide temperatures are brought instantaneously to 4.2 K. This mimics the transfer of liquid ^{4}He into a cryostat that has been pre-cooled using liquid N_2.

Requiring that the power entering and leaving each junction are equal generates a system of four coupled differential equations:

$$P_1 + P_5 = P_2 + P_4, \tag{5.1a}$$

$$P_3 = P_2 + P_6, \tag{5.1b}$$

$$P_3 + P_{10} = P_7 + P_8, \tag{5.1c}$$

$$P_9 = P_4 + P_8 + P_{11}. \tag{5.1d}$$

Next we write the powers in terms of thermal conductances and heat capacities as

follows:

$$P = \Delta T G(T), \tag{5.2a}$$

$$P = \frac{\mathrm{d}}{\mathrm{d}t}\left(T(t)C_V(T)\right), \tag{5.2b}$$

and then numerically solve Eqs. 5.1 using Mathematica 4.0. For copper, over the temperature range considered here, both phonon and electron contributions to the total heat capacity need to be considered. The phonon contribution is described by the Debye model and the electronic contribution, which becomes important below 10 K comes from considering thermally activated electrons near the Fermi surface. See Appendix B for a discussion of the heat capacity of copper. The thermal conductivity of stainless steel is approximately linear in temperature over the full temperature range with coefficient 0.141 $\mathrm{Wm^{-1}K^{-2}}$. The cooling rate of the filters is expected to be highly independent on the value chosen for the thermal conductivity of the silver wire. We use the low temperature value of $\kappa_{\mathrm{Ag}} = 15.83T$ $\mathrm{WK^{-1}kg^{-1}}$ over the entire temperature range. Changing the value of the coefficient of κ_{Ag} by two orders of magnitude produces a change of 15% in cooling rate of the filters. The cooling rate is more sensitive to the thermal conductivity of the vespel, but the low-temperature value given by Locatelli [21] is used over the entire temperature range. Fig. 5.6 is a plot of the numerically determined cooling rates of T_1 and T_2 from Fig. 5.4. These results are compared to the observed cooling rate starting from 77 K down to 4.2 K. The agreement between the numerical and experimental data is reasonably good. Notice that the filters take over 3.5 hours to reach liquid ^{4}He temperature. To speed up the cooling 50 mTorr of H_2 exchange gas can be introduced into the vacuum space surrounding the filters. At approximately 13 K the H_2 gas will freeze, restoring the high vacuum. This will substantially reduced the cool down time.

In the dilution fridge experiment the interior of the vacuum can is filled with ^{4}He exchange gas until a temperature of 8 K is reached at which point the can is evacuated. Thus, it is crucial to know the cooling rate of the filters from 8 K to the base temperature of the fridge $\sim$ 50 mK. Fig. 5.7 shows the numerical results of this calculation. The inset is a detailed view of the cooling curves as their equilibrium values are approached. The equilibrium temperatures reached by the various stages are $T_1 = T_2 = T_4 = 57$ mK and $T_2 = 69$ mK. This calculation was also carried out for the single pole filter of the reference stage. Using equivalent definitions for the temperatures as seen in Fig. 5.4 for the sample side we find that the equilibrium temperatures achieved are $T_1 = T_3 = 76$ mK and $T_4 = 83$ mK.

5.3 DC Analysis

Before proceeding to numerically calculate the filter performance it is instructive to first solve the DC problem. The numerically calculated equilibrium temperatures from the previous section should agree with the temperatures obtained from the DC solution.

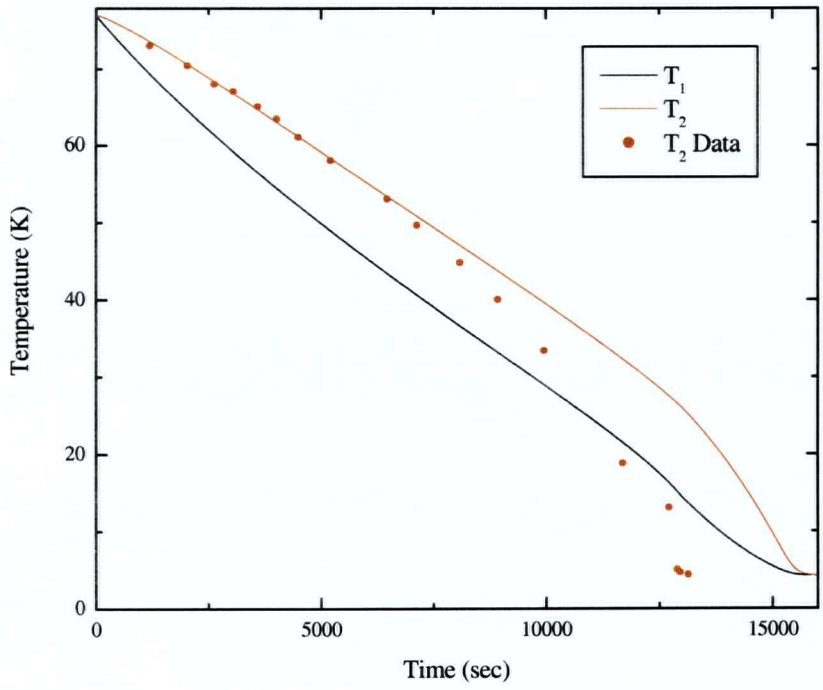

Figure 5.6: Cooling curve of the sample filter: measured (dots) versus simulation results.

As with ordinary circuit analysis the capacitance plays no role in determining the long term steady-state solution so that the capacitors in Fig 5.5 can be ignored leading to the circuit pictured in Fig 5.8 (For simplicity in this analysis it is assumed that $T_s \approx T_1$). From this circuit it is easy to set-up a system of three equations to solve for the three unknowns, P_1, P_2, and P_3:

$$T_{wg} - P_1(G_{vp2}^{-1} + G_{ss1}^{-1}) - P_2(G_{vp1}^{-1} + G_{Ag2}^{-1} + G_{ss2}^{-1}) = T_{mc} \quad (5.3a)$$

$$T_{wg} - P_1(G_{vp2}^{-1} + G_{ss1}^{-1}) - P_3 G_{Ag1}^{-1} = T_{mc} \quad (5.3b)$$

$$P_3 G_{Ag1}^{-1} - P_2(G_{vp1}^{-1} + G_{Ag2}^{-1} + G_{ss2}^{-1}) = 0 \quad (5.3c)$$

The difficulty comes in, however, because calculating values for the various thermal conductances requires knowledge of T_1, T_2, T_3 and T_4, which are the temperatures we are trying to calculate in the first place. The low temperature thermal conductivities of both stainless steel and silver are linear in temperature so that $G_{ss/Ag} = (A/l)\kappa_{ss/Ag}(\bar{T})$ where $\bar{T}$ is the average temperature across the material. The thermal conductivity of vespel depends on the square of the temperature, but provided the temperature difference across the vespel is not too large $G_{VP} \approx (A/l)\kappa_{VP}(\bar{T})$. Assuming that $T_1 \approx T_2 \approx T_3 \approx 50$ mK and $T_4 \approx 700$ mK leads to powers of $P_1 = P_3 = 0.25$ μW and $P_2 = 0.18$ nW. These powers can in turn be substituted back into the original equations to calculate new values for the unknown temperatures yielding $T_1 = 55$ mK, $T_2 = T_3 = 56$ mK, and $T_4 = 68$ mK. This process can be

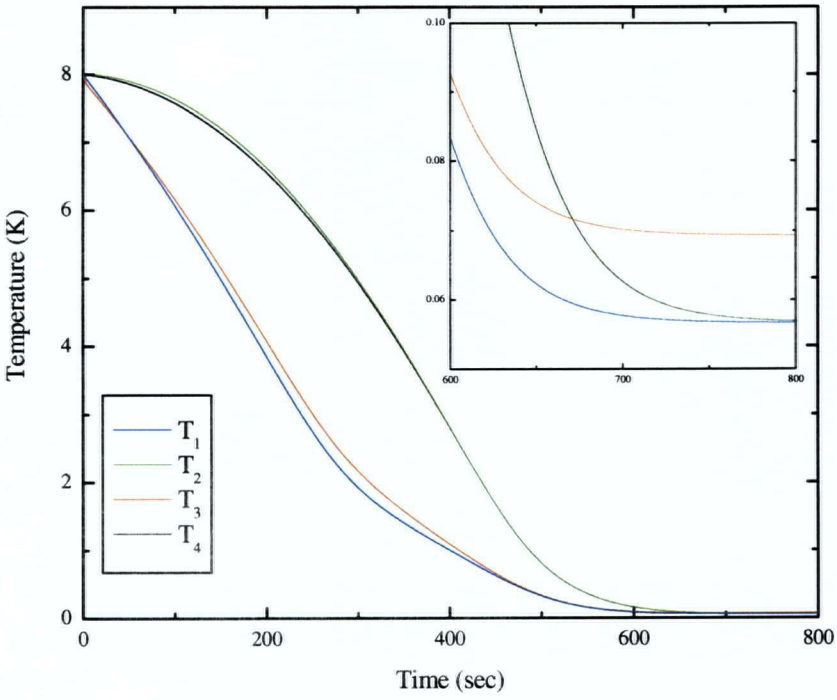

Figure 5.7: Cooling curves of the sample filter and thermal stage from 8 K to ≈ 50 mK.

repeated until a self consistent solution is reached. It turns out that the temperatures barely change after just one iteration. The final equilibrium temperatures (after four iterations) are $T_1 = T_2 = 55$ mK, $T_3 = 56$ mK, and $T_4 = 66$ mK. Comparing the results of the full time-dependent analysis of §5.2 we find excellent agreement and gain confidence in the numerical methods employed. The same analysis was performed on the reference side yielding temperatures of $T_1 = T_3 = 73$ mK and $T_4 = 78$ mK, again these values are in good agreement with those from the numerical calculation.

5.4 Numerical Calculations

In the final section of this chapter the equivalent circuit model is used to numerically calculate the temperature stability of the reference and sample thermal stages when the mixing chamber temperature is allowed to fluctuate as $T_{mc} = T_0 + T^* \cos \omega t$, where $T_0 = 50$ mK is the average temperature of the mixing chamber, T^* is the amplitude of the oscillations, and ω is the angular frequency of the temperature oscillations. These calculations are then repeated for the case where the waveguide temperature T_{wg} is made to fluctuate.

In our experiments the microwave power is typically modulated at 1 Hz and so in the calculations presented below it is the temperature fluctuations at 1 Hz that are relevant. The amplitude of the fluctuations at any point in the thermal circuit can

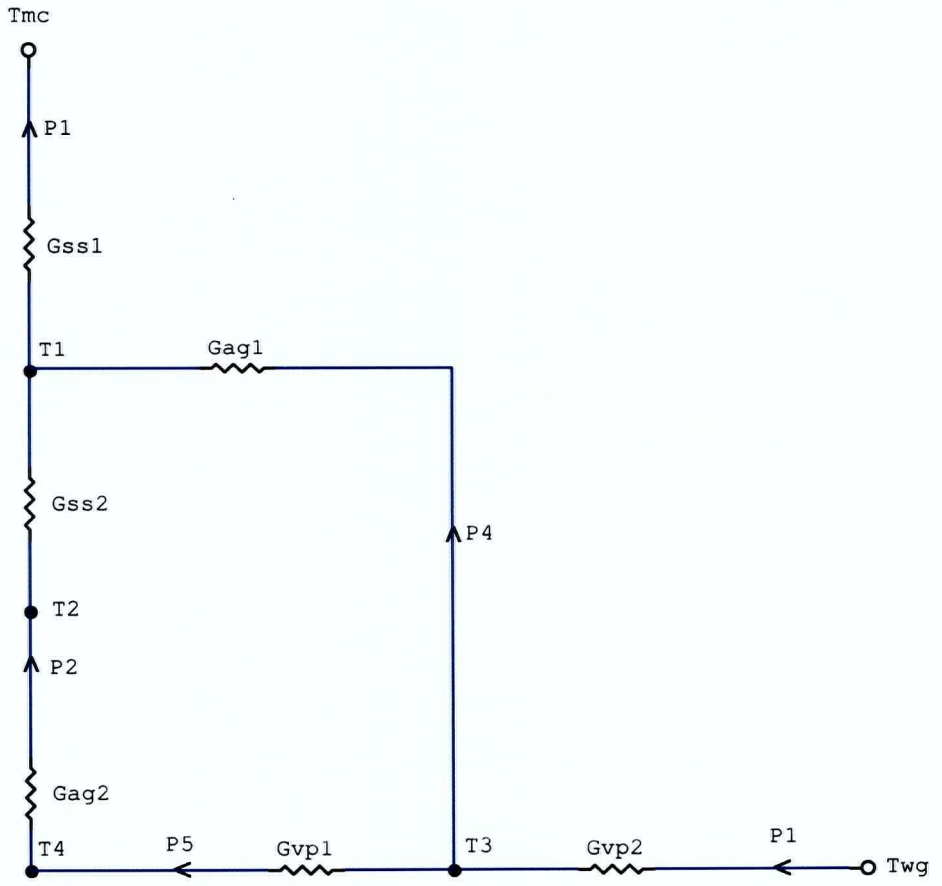

Figure 5.8: DC equivalent circuit of the thermal design shown in Fig 5.5.

be found by Fourier transforming the temperature at that point in the following way:

$$|T| = \left| \frac{\omega}{2\pi} \int_{t_0}^{t_0+2\pi/\omega} T(t) e^{i\omega t} dt \right|. \tag{5.4}$$

The first calculation was performed by allowing the mixing chamber temperature to fluctuate at 1 Hz with an amplitude of 10 mK. The results of the calculation are:

$$\left| \frac{T_1}{T_{mc}} \right| = 1.6 \times 10^{-2}, \tag{5.5a}$$

$$\left| \frac{T_2}{T_{mc}} \right| = 2.2 \times 10^{-4}, \tag{5.5b}$$

$$\left| \frac{T_4}{T_{mc}} \right| = 1.9 \times 10^{-4}. \tag{5.5c}$$

Eq. 5.5a implies that the 10 mK oscillation at the mixing chamber appears as a 2 μK oscillation at T_4. These values for $|T_1/T_{mc}|$ and $|T_2/T_{mc}|$ can be compared to $\omega^{-1}\tau_1^{-1} = 1.9 \times 10^{-2}$ and $\omega^{-2}\tau_1^{-1}\tau_2^{-1} = 2.7 \times 10^{-4}$ respectively, both giving reasonably

good agreement. The fluctuation suppressions implied by Eqs. 5.5 should be essentially independent of the size of the thermal fluctuations for small fluctuations and this was verified by repeating the numerical calculations using $T^{\star} = 5$ mK. Next, the waveguide temperature ($T_0 = 700$ mK) was made to have a 1 Hz temperature fluctuation of 25 mK resulting in $|T_3/T_{wg}| = 4.2 \times 10^{-2}$ and $|T_4/T_{wg}| = 2.1 \times 10^{-5}$ which can be compared to 1.7×10^{-2} and 3.2×10^{-4} obtained from §2.4. Notice that the results for $|T_3/T_{wg}|$ are close, but that there appears to be some extra suppression of the temperature fluctuations at T_4 in the numerical calculation. This additional filtering is due the second stage of the cascaded low-pass filters suspended from the mixing chamber. These calculations were also performed for the reference side. A one Hz fluctuation of the mixing chamber was suppressed by a factor of $|T_4/T_{mc}| = 1.5 \times 10^{-2}$ and fluctuations of the waveguide temperature by $|T_4/T_{wg}| = 2.0 \times 10^{-3}$.

Chapter 6

Future Considerations

The final chapter of the thesis briefly reviews a few of the upcoming projects for the new low-temperature microwave spectrometer. First a new detection scheme that is expected to improve the measurement sensitivity by up to a factor of 10^2 is discussed. This is followed by an introduction to some of the experiments that are planned for the new apparatus. The first is an absorption measurement investigating Andreev bound states and will be performed in a liquid ^{4}He cryostat. The other measurements are intended for a ^{3}He/^{4}He dilution fridge and include a systematic examination of low energy quasiparticle scattering dynamics that will compliment the work already completed at higher temperatures, plus microwave conductivity measurements of unconventional heavy fermion superconductors.

6.1 Detection System

The detection system currently employed shows excess noise in both the bolometer itself and in the electronics used to amplify the signals before processing. Turner *et al.* have measured 40 dB of excess noise in the Cernox bolometers in the presence of a constant 1.3 μA bias current [1]. These authors speculate that the source of this excess noise is generation-recombination noise that can occur if there are energy level traps from defects or impurities within the semiconducting bandgap. Haller-Beeman Associates Inc. produce single crystal semiconducting samples that have been prepared by a process known as neutron transmutation doping (NTD) which minimizes generation-recombination noise. Preliminary measurements of the noise spectrum of these Haller-Beeman sensors show no excess noise under constant current bias. The present method used to generate the bias current in the bolometer uses an interchangeable bias resistor in series with the bolometer, a voltage is then applied across the pair of resistors using a battery. In the present scheme the bias resistor is at room temperature ($\sim$ 300 K) resulting in a substantially higher thermal (Johnson) noise than would be encountered if the bias resistor was cooled to the base temperature of the experiment ($\leq$ 1.2 K). Ideally one would have a small bank of bias resistors cooled in the experiment and some method of electronically selecting certain combinations of these resistors, using reed relays for example, to produce the desired bias resistance. The current detection technique can be further optimized through a careful selection of ultra-low-noise amplifiers used to magnify detected signals by a factor of 10^4.

In addition, work has begun on the development of an alternative detection scheme. The current technique uses lock-in detection to measure the temperature rise of a sample exposed to low-frequency modulated microwave magnetic field. This requires that a temperature dependent calibration factor to convert this temperature

rise to absolute power has to be determined prior to each frequency scan. The new detection scheme will employ a square wave modulation of the microwaves, and rather than measuring the temperature rise of the sample, a feedback loop will be used to pass a current through the chip heater to null the bolometer response. In other words, during the half cycle that the microwaves are on, the thermal stage will reach some stable temperature T_B, then during the second half of the cycle when the microwaves are off a current will be passed through the heater such that the temperature T_B is maintained. This procedure will be repeated at each step of the frequency scan. At each step the heater current I_H is measured and the desired power is given by $I_H^2 R_H$ where R_H is the heater resistance. Thus rather than establishing a calibration factor prior to each frequency scan, all that is required is one careful temperature calibration of the heater resistance. In the detection technique currently used, if there is a small temperature drift during a frequency scan the sensitivities of the thermal stages change and the calibration factor measured at the beginning of the frequency sweep is inaccurate. Since the heater resistance is nearly temperature independent the new detection technique will be insensitive to small temperature drifts. This detection method will be fully automated and furthermore will make use of a scheme to optically isolate the detection equipment from external sources of noise that can enter, for example, by ground loops.

6.2 Andreev Bound States Experiment

Andreev reflections occur when one tries to pass current through a normal metal-superconductor junction (denoted NS). If quasiparticles incident from the normal metal side have insufficient energy to overcome the superconducting gap they cannot penetrate into the superconductor, nevertheless a current will flow across the junction when a sub-gap voltage is applied. Andreev reflections provide the mechanism for current flow and a qualitative description of this process follows. When a low energy quasi-electron which is unable to surmount the superconducting gap is incident on the NS junction, if it is to cross the interface, it has no choice but to join the superconducting condensate. To accomplish this it must form a Cooper pair with a second quasi-electron. The only available electrons exist in the Fermi sea and lie at the Fermi energy. Once joined with the second quasi-electron the Cooper pair can cross the junction. The act of "pulling" an electron from the Fermi surface leaves behind a quasi-hole that has momentum *opposite* that of the original quasi-electron. Because the hole has the opposite charge and velocity of the original electron it carries the same current that was present prior to the forming of the Cooper pair. Hence a current flows across the junction. An analogous situation occurs when a low energy quasi-hole is incident on the NS interface. In this case a Cooper pair from the superconducting side is broken apart and one of the quasi-electrons fills the hole in the Fermi sea while the second travels through the normal metal with momentum opposite that of the incident quasi-hole.

A so-called Andreev bound state can be formed when a normal metal layer is deposited onto the surface of a superconductor. The thickness d of the normal metal

is chosen to be much less than the metal's mean free path l. Low energy quasi-electrons(holes) incident on the NS junction undergo Andreev reflections as described above and the reflected quasi-hole(electron) travels through the metal and experiences the usual specular reflection at the free surface of the metal. In specular reflections the nature of the quasiparticle is not altered and only the perpendicular component of the momentum is reversed. See Fig. 6.1 for a cartoon sketch contrasting Andreev and specular reflections. This specularly reflected quasiparticle is re-incident on the

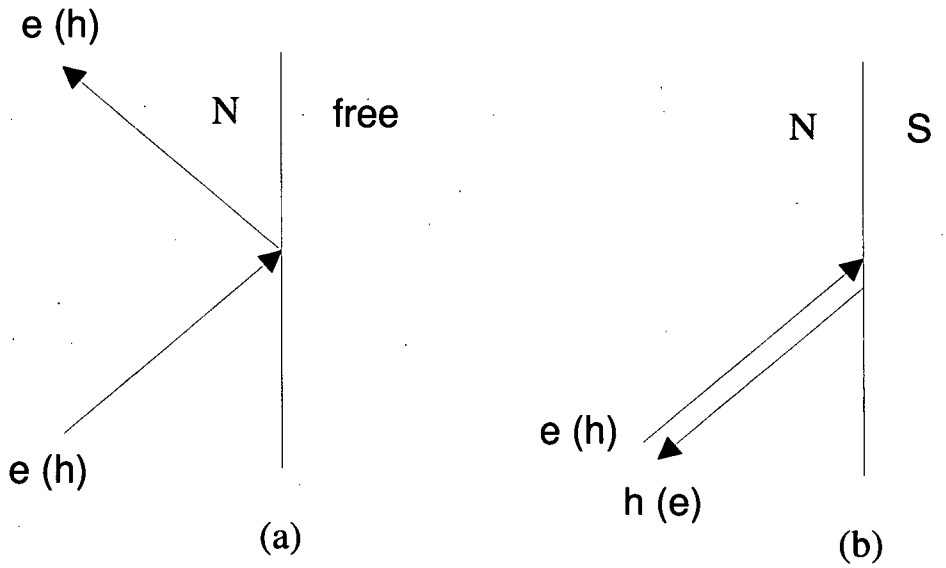

Figure 6.1: Schematic of a (a) specular reflection and (b) Andreev reflection. In the specular reflection only the velocity component perpendicular to the NS interface is reversed, while in the Andreev reflection both velocity components are reversed and the reflected quasi-electron(hole) is converted into a quasi-hole(electron)

NS junction and undergoes a second Andreev reflection ..., the process repeats indefinitely and a bound state is formed (see Fig. 6.2).

In 1994 Chia-Ren Hu published an article in which he demonstrated that a superconductor with $d_{x^2-y^2}$ symmetry, having a π phase shift between the different lobes of the order parameter, cut to expose the $\{110\}$ surface has Andreev bound states with zero energy relative to the Fermi energy. Furthermore, he showed that these zero energy states are present even in the limit the that the normal layer thickness $d \to 0$ [26]. The presence of these zero energy states adds a δ-function contribution to the quasiparticle density of states $N(\epsilon)$, and should be observable by any measurement sensitive to the energy dependence of $N(\epsilon)$. For example, the δ-function term of $N(\epsilon)$ adds a $1/T$ contribution to $\Delta\lambda(T)$. Carrington *et al.* have measured the temperature dependence of $\Delta\lambda(T)$ and saw an upturn at low temperatures in crystals of $YBa_2Cu_3O_{6.9}$ cut to expose $\{110\}$ surfaces [27].

There two degenerate zero energy bound states corresponding to currents cir-

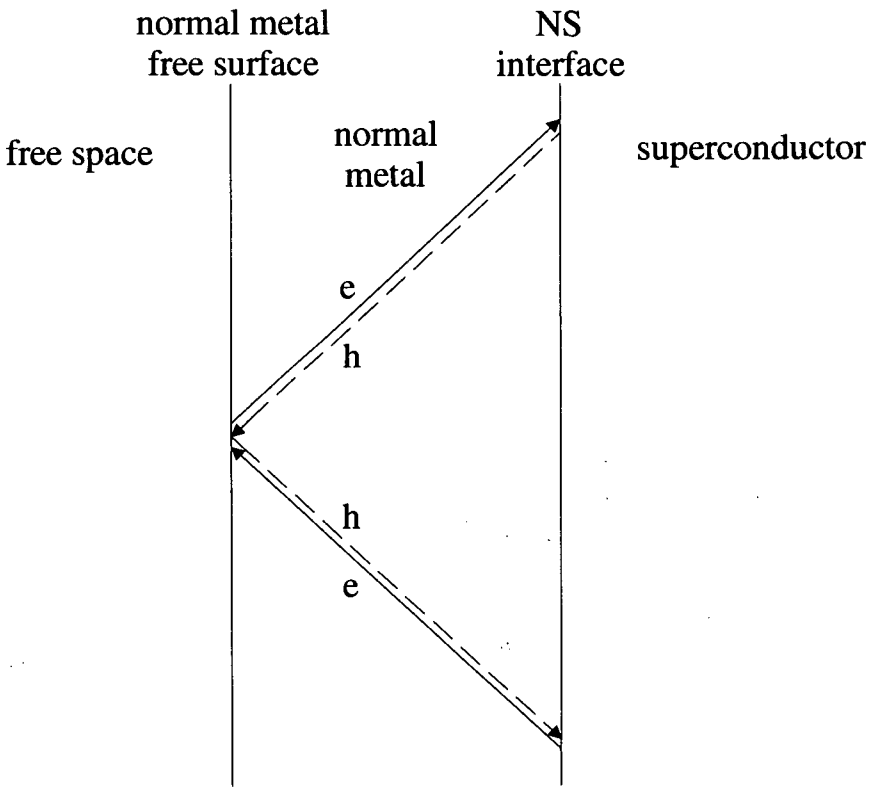

Figure 6.2: Schematic of an Andreev bound state. "e" indicates an electron-like quasiparticle (solid line) and "h" is a hole-like quasiparticle (dashed line).

culating in opposite directions. These states can be split by applying a small DC magnetic field. This splitting can be probed in a broadband electron spin resonance (ESR) type experiment in which the sample is exposed to electromagnetic radiation whose frequency is continuously varied. This splitting should be observed as an absorption peak whose centre frequency is proportional to the size of the DC field. One could then measure the temperature and field dependence of the broadening of the absorption peak [28]. This measurement can be performed using the new microwave spectrometer in a pumped liquid ^{4}He cryostat. In §2.2 the advantages of applying a superconducting coating to the interior of the waveguide structure were discussed, but this coating was avoided in the new apparatus to allow for the possibility of performing measurements, such as this one, with an externally magnetic field.

6.3 Low-Energy Quasiparticle Scattering Dynamics

Turner *et al.* [17] have successfully applied the bolometric technique to a broadband measurement of the microwave absorption of $YBa_2Cu_3O_{6+y}$ for temperatures ranging from 1.2 to 10 K. These measurements have resulted in the first observation of the

cusp-like line shape predicted for the conductivity of a d-wave superconductor for weak (Born) limit quasiparticle scattering [17]. The experimental results have been compared to theoretical models developed by Hirschfeld *et al.* that are based on the so-called self-consistent t-matrix approximation (SCTMA) [29, 30]. A product of these models is an expression for the microwave conductivity $\sigma(\omega, T)$ that has an energy-averaged Drude form:

$$\sigma(\omega, T) = \frac{ne^2}{m^\star} \left\langle \frac{1}{i\omega + 1/\tau(\epsilon, T)} \right\rangle_\epsilon , \tag{6.1}$$

where $1/\tau(\epsilon, T)$ is an energy- and temperature-dependent scattering rate and $\langle ... \rangle_\epsilon$ denotes an energy average weighted by the quasiparticle density of states $N(\epsilon)$. Hirschfeld *et al.* have shown that $\tau^{-1}(\epsilon) \approx \Gamma_B \epsilon$ for weak-limit Born scattering and that $\tau^{-1}(\epsilon) \approx \Gamma_u/\epsilon$ in the strong, or unitary, scattering limit [30]. Furthermore, these authors showed that in the presence of unitary scatterers, the density of states of a d-wave superconductor is substantially modified giving rise to a residual quasiparticle density at low energies. In contrast, in the weak scattering limit a residual density of states is seen only at exponentially small energies. A consequence of the residual density of states for unitary scattering is a T^2 temperature dependence of $\Delta\lambda(T)$, whereas for Born scattering $\Delta\lambda(T) \propto T$. In 1993 Hardy *et al.* were the first to report measurements of a linear temperature dependence of $\Delta\lambda(T) = \lambda(T) - \lambda(1.3\text{ K})$ at low temperatures on very pure samples of $YBa_2Cu_3O_{6.95}$ [31]. This result was the first strong piece of evidence supporting the notion that the superconducting gap has nodes, moreover, a linear temperature dependence of $\Delta\lambda(T)$ at low temperatures is a strong indication that the samples are in the weak-scattering limit. Further evidence supporting this claim came shortly after in 1994 from Bonn *et al.* performed a systematic investigation of impurity effects on $YBa_2Cu_3O_{6.95}$ [32]. These authors intentionally doped Zn and Ni impurities, both of which substitute for Cu in the CuO_2 planes, into their samples and observed the effects on physical properties such as $\Delta\lambda(T)$. They found that when the dopant was Ni, $\Delta\lambda(T)$ retained its linear temperature dependence up to a 0.75% substitution, while substantially lower amounts of Zn substitution caused a cross-over to the quadratic behaviour expected for strong impurity scattering. These results were explained by recognizing that Zn is a strong pair-breaking scatterer, whereas Ni, which is a magnetic impurity, has no pair-breaking effect.

The conductivity measurements by Turner *et al.* [17] have been performed on single crystals of $YBa_2Cu_3O_{6+y}$ at two separate oxygen contents, namely ortho-II ordered $YBa_2Cu_3O_{6.52}$ and fully doped $YBa_2Cu_3O_{6.99}$. Although both dopings exhibit the characteristic cusp-like line shape expected for a d-wave superconductor, the discussion here will be limited to the ortho-II ordered sample and those findings that are at odds with theoretical predictions will be emphasized and in particular those that can be further investigated using the newly developed low-temperature microwave spectrometer. Fig. 6.3 is a plot of the $\hat{a}$-axis surface resistance versus frequency for the ortho-II ordered sample at four different temperatures. The $\hat{a}$-axis conductivity is obtained from the surface resistance data via Eq. 1.10a using

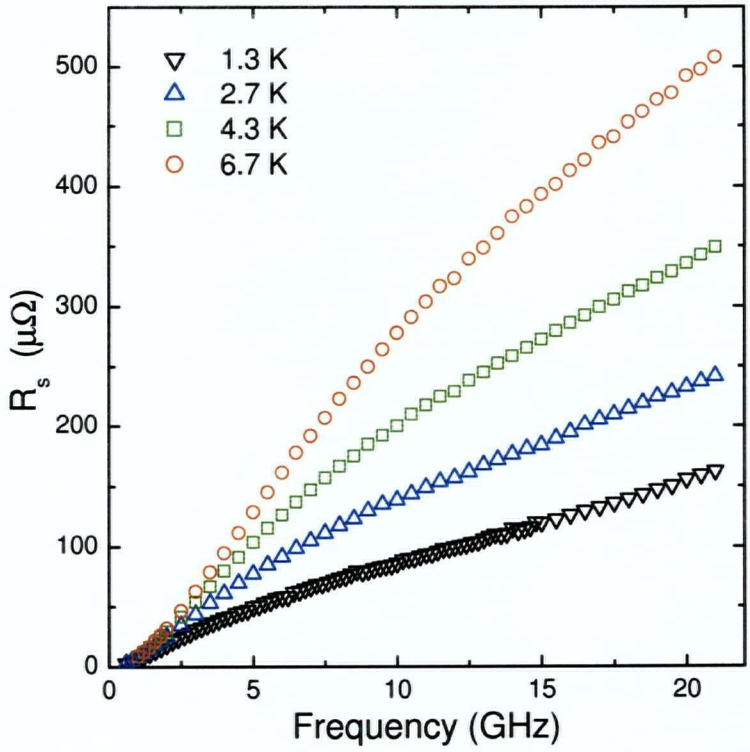

Figure 6.3: Low temperature surface resistance data for the $\hat{a}$-axis direction of ortho-II ordered $YBa_2Cu_3O_{6.52}$.

the recently determined value of $\lambda_a = 202 \pm 22$ nm for the ortho-II ordered $\hat{a}$-axis penetration depth [18] and is shown in Fig. 6.4. The 6.7 K data has been fit to Eq. 6.1 using the Born limit form of $\tau^{-1}(\epsilon) = \Gamma_B \epsilon$. The fit is extremely good over the entire frequency range with fitting parameters $\hbar\Gamma_B = 0.032$ and $ne^2\hbar/(m^\star\Delta_0) = 1.26 \times 10^6\ \Omega^{-1}\mathrm{m}^{-1}$. When these parameters are used to generate curves for the lower temperature data sets, we find that the Born-limit model underestimates the spectral weight as the temperature is decreased. The SCTMA model requires that the conductivity scale as ω/T, but as seen in the inset of Fig. 6.4 the data obey an alternative scaling law given by $\omega/(T + T_0)$ with $T_0 = 2$ K. Thus, these data indicate a residual quasiparticle conductivity at zero temperature in stark contrast to theoretical predictions.

As discussed in §1.4 the frequency integrated quasiparticle conductivity is a measure of the temperature dependent normal fluid density and the superfluid density is given by $1/\lambda^2(T)$. The two-fluid model requires that oscillator strength lost in the superfluid must reappear in the normal fluid. In order to integrate the quasiparticle conductivity, the data are first fit to the following phenomenological model:

$$\sigma_1(\omega) = \frac{\sigma_0}{1 + (\omega/\Gamma)^y}, \tag{6.2}$$

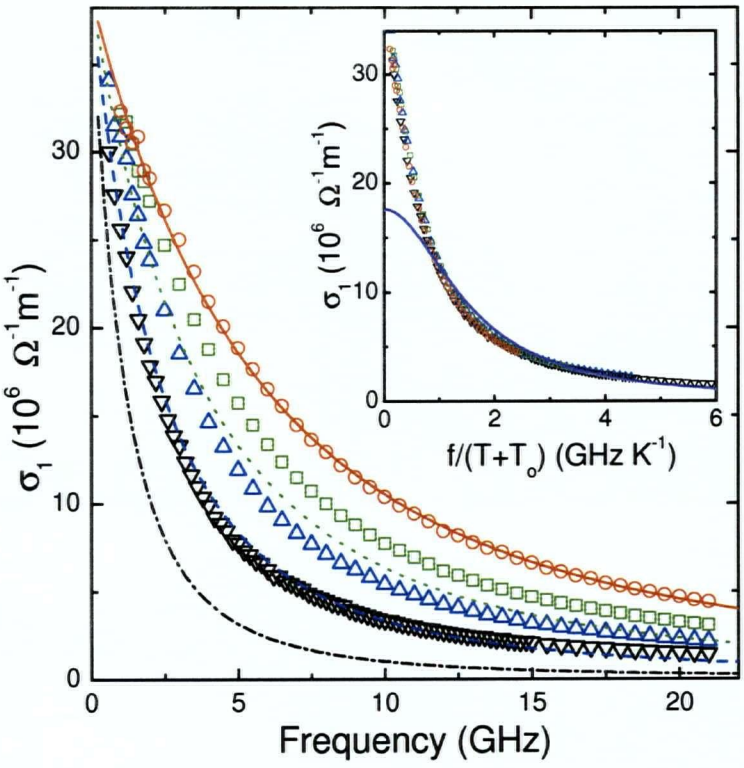

Figure 6.4: The frequency and temperature dependent conductivity of ortho-II ordered $YBa_2Cu_3O_{6.52}$ extracted from surface resistance data of Fig. 6.3. The solid line is a fit to the 6.7 K data using a theoretical model for Born-scattering. Using the parameters from the 6.7 K fit the dashed lines are predictions for the three lower temperatures; clearly the model fails to capture the observed temperature dependence. The inset shows an unusual scaling behaviour obeyed by the data.

where σ_0, Γ, and y are fit parameters. The fits to the data are extrapolated to high frequencies allowing an approximate integration of the conductivity over all frequencies. Fig. 6.5 shows the individual fits to the data and the inset compares the integrated quasiparticle conductivity to independent measurements of the loss of superfluid density obtained from $\Delta\lambda(T)$. The agreement of the slopes of the temperature dependent normal fluid density and loss of superfluid density indicate that the oscillator strength sum rule is obeyed and hence confirms that the extrapolated phenomenological model properly captures the quasiparticle oscillator strength residing at frequencies exceeding the measurement bandwidth. Tracing the integrated conductivity down to $T = 0$ K again reveals a residual normal fluid density.

Measurements of $\sigma_1(\omega, T)$ at lower temperatures are critical to further examine the unusual scaling of the data and apparent residual normal fluid density at $T = 0$ K. The new low-temperature spectrometer has been engineered specifically to address this issue.

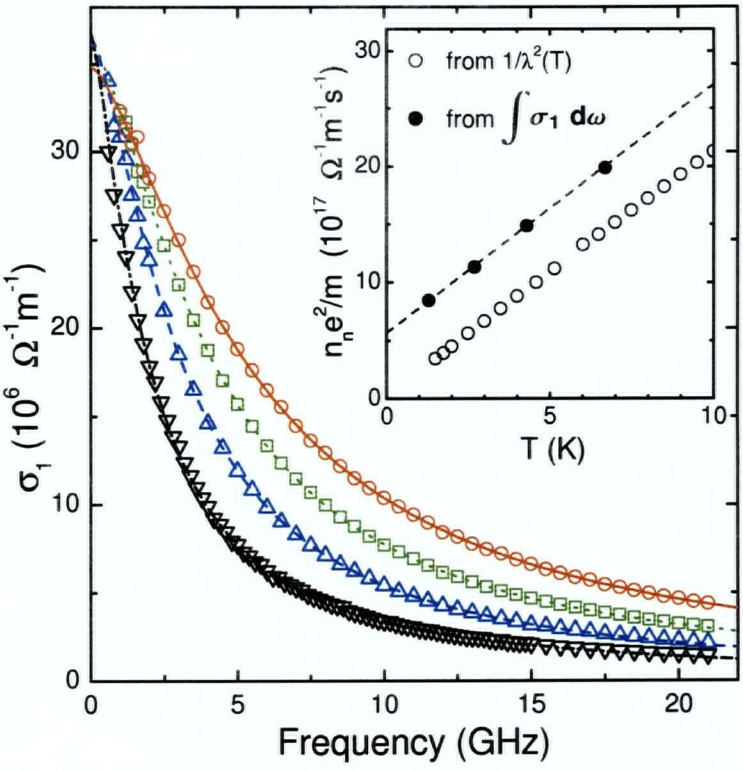

Figure 6.5: The solid lines are fits to the data using Eq. 6.2. The inset compares the normal fluid density obtained by integrating $\sigma_1(\omega)$ to the loss of superfluid density inferred from 1.1 GHz $\Delta\lambda(T)$ data. The slope of the dashed line equals that of the open symbols indicating that the oscillator strength sum rule is obeyed, however extrapolating the integrated $\sigma_1(\omega)$ to $T = 0$ K reveals a residual normal fluid density.

Another issue that has yet to be satisfactorily examined, despite being in the literature for over a decade now, is the universal conductivity of a d-wave superconductor predicted by Patrick Lee [33]. In 1993 Lee published an article in which he predicted that the residual conductivity $\sigma(\omega \to 0, T \to 0)$ of a d-wave superconductor tends to a non-zero result that is independent of impurity concentration and is given by $\sigma_{00} = ne^2/[m\pi\Delta_0(0)]$, where $\Delta_0(0)$ is the maximum gap at $T = 0$ K. This effect arises as a result of the competition between the growth of the normal fluid density with increasing impurity concentration and a corresponding reduction in the scattering mean free path. In principle this effect is independent of the scattering strength, however in the Born limit, universal conductivity is only expected at exponentially small temperatures [30]. In YBCO one can access the unitary scattering regime by intentionally doping Zn impurities in to the CuO_2 planes as discussed above. To date no experiment has had the necessary resolution to adequately test the universal electrical conductivity, although a related limit has been investigated in DC thermal conductivity measurements made by Taillefer *et al.* in 1997 [34]. These authors report

a residual thermal conductivity in samples of $YBa_2Cu_3O_{6+y}$ that is independent of Zn impurities with concentrations ranging from 0% to 3% of Cu.

Subsequently, in 2000 a second paper appeared in which Durst and Lee improve upon the results of [33] by including so-called vertex and Fermi-liquid corrections [35]. The results of these corrections are that while the thermal conductivity maintains its universal value, both vertex and Fermi-liquid corrections modify the electrical conductivity. Vertex corrections take into account that forward and back scattering can have different effects on the progress of a charge carrier and depend on the nature of the impurity scattering. Fermi-liquid corrections account for Fermi-liquid interactions between electrons in the superconductor and depend on the strength of the interactions [35].

Finally, we mention a recent result from the group of Louis Taillefer at Université de Sherbrooke. They measured the electronic contribution to the thermal conductivity in a single crystal of $YBa_2Cu_3O_{6.99}$ that was grown at UBC. Their measurements were performed in a $^3He/^4He$ dilution refrigerator and span a temperature range of 50 mK to 600 mK. These authors compared their data to theoretical predictions for both weak-limit Born scattering and strong unitary scattering. They found that in both of these extreme cases the theoretical models gave an inadequate description of the data, leading these authors to speculate that they are in an intermediate scattering regime [36]. Measurements of the electrical conductivity at UBC at 1 K and above also indicate that the data are best described using intermediate scattering interpretations. It will be very interesting to track the behaviour of the quasiparticle scattering as temperature is further reduced.

A broadband measurement of the electrical conductivity is essential to provide a complete picture of the low-temperature quasiparticle dynamics. Reasonable estimates of the parameters appearing in σ_{00} (prior to the above mentioned corrections) requires that a measurement of the surface resistance at a frequency f in GHz have a resolution better than $R_s \approx 5 \times 10^{-8} f^2$ in order to observe universal conductivity [11]. At 1 GHz this corresponds to a surface resistance resolution of better than 50 nΩ, which is well within the targeted sensitivity of the new low-temperature apparatus. Comparing microwave data of the low-temperature, low-frequency electrical conductivity to the universal-limit of thermal conductivity obtained by Taillefer *et al.* [34] will provide many new insights into the low energy quasiparticle dynamics in YBCO.

6.4 Heavy Fermion Superconductors

There are a variety of novel experiments that can be performed on heavy fermion superconductors using the low-temperature microwave spectrometer. The conductivity of common metals typically follows the Drude model description as presented in §1.4:

$$\sigma(\omega) = \sigma_1 - i\sigma_2 = \left(\frac{ne^2}{m}\right)\frac{1}{\Gamma - i\omega}, \tag{6.3}$$

where Γ is a frequency independent scattering rate. At high temperatures heavy fermion materials also adhere to this description, however at low temperatures their

behaviour is drastically altered due to the onset of strong electron correlations. As temperature is reduced below a coherence temperature $T^\star$ these materials show a large increase in magnetic susceptibility and the electronic contribution to the specific heat. These effects are normally explained as an enhancement of the effective mass $m^\star$ which can be of the order of $100m_e$ where m_e is the free electron mass. The mass enhancement renormalizes the plasma frequency $(\omega_p^\star)^2 = 4\pi ne^2/m^\star$ shifting the electronic excitations, characterized by an effective scattering rate $\Gamma^\star$, to low energies. As the temperature drops further below $T^\star$, $m^\star$ continues to increase while $\Gamma^\star$ decreases. To track the energy dependence of the renormalization effects one uses a frequency dependent scattering rate $\Gamma^\star(\omega)$ and effective mass $m^\star(\omega)$ in Eq. 6.3 to interpret the observed conductivity spectrum. Many of the interesting features, such as the renormalized Drude peak, are expected to reside within the microwave frequency regime making the low-temperature microwave spectrometer the ideal apparatus to investigate the conductivity of many heavy fermion materials [37].

Once cooled below the superconducting transition temperature T_c (typically $\leq 1\ K$) heavy fermion materials may exhibit absorption peaks in surface resistance measurements due to order-parameter collective modes. These collective modes are due to macroscopic quantum oscillations of the pair condensate and can be excited by ultrasound or electromagnetic waves. It is thought that the heavy fermion materials may be characterized by unconventional ^{3}He-like order parameters and theoretical predictions of mode frequencies for various order parameter symmetries have been made [38]. Characteristic frequency scales in these materials are determined by the gap function $\Delta/\hbar \sim k_B T_c/\hbar \approx 20$ GHz for $T_c = 1$ K. Feller *et al.* have observed collective modes in surface resistance measurements of UBe_{13} by cavity perturbation techniques [39]. The broadband apparatus will resolve the shape of these modes in much greater detail and allow for a systematic investigation of their temperature dependence. While evidence for collective modes in UBe_{13} does seem to exist, it is lacking for other heavy fermion materials such as UPt_3.

Bibliography

[1] P. J. Turner, D. M. Broun, Saeid Kamal, M. E. Hayden, J. S. Bobowski, R. Harris, D. C. Morgan, J. S. Preston, D. A. Bonn, and W. N. Hardy. Bolometric technique for high-resolution broadband microwave spectroscopy of ultra-low-loss samples. *Rev. Sci. Instrum.*, 75:124, 2004.

[2] R.J. Corruccini and J. J. Gniewek. *Specific Heats and Enthalpies of Technical Solids at Low Temperatures.* U.S. Department of Commerce National Bureau of Standards, Washington D.C., 1960.

[3] M. Tinkham. *Introduction to Superconductivity, Second Ed.* McGraw-Hill, Inc., New York, 1996.

[4] Private communication with R. Liang.

[5] M. Grüninger PhD thesis, 1999.

[6] R. Liang, P. Dosanjh, D. Bonn, D. Baar, J. Carolan, and W. Hardy. Growth and Properties of Superconducting YBCO Single Crystals. *Physica (Amsterdam)*, 195C:51, 1992.

[7] R. Liang, D. Bonn, and W. Hardy. Growth of high quality YBCO single crystals using $BaZrO_3$ crucibles. *Physica (Amsterdam)*, 304C:105, 1998.

[8] R. Liang, D. Bonn, and W. Hardy. Preparation and X-ray characterization of highly ordered ortho-II phase $YBa_2Cu_3O_{6.50}$ single crystals. *Physica (Amsterdam)*, 336C:57, 2000.

[9] C.C. Tsuei and J.R. Kirtley. Pairing symmetry in cuprate superconductors. *Rev. Mod. Phys.*, 72:969, 2000.

[10] J.F. Annett *et al.* in *Physical Properties of High Temperature Superconductors, Vol V.* edited by D. Ginsberg, World Scientific Publishing Co. Pte. Ltd., Singapore, 1996.

[11] D. Bonn and W. Hardy. in *Physical Properties of High Temperature Superconductors, Vol V.* edited by D. Ginsberg, World Scientific Publishing Co. Pte. Ltd., Singapore, 1996.

[12] H. Weinstock and M. Nisenoff. *Microwave Superconductivity.* Kluwer academic Publishers, Netherlands, 1999.

[13] D. J. Griffiths. *Introduction to Electrodynamics, Second Ed.* Prentice-Hall, Inc., New Jersey, 1989.

[14] J. D. Jackson. *Classical Electrodynamics, Third Ed.* John Wiley & Sons, Inc., New York, 1999.

[15] R. Ormeno, D. Morgan, D. Broun, S. Lee, and J. Waldram. Sapphire Resonator for the Measurement of Surface Impedance of High-Temperature Superconducting Thin Films. *Rev. Sci. Instrum.*, 68:2121, 1997.

[16] A. Hossenini, R. Harris, S. Kamal, P. Dosanjh, J. Preston, R. Liang, W. Hardy, and D. Bonn. Microwave Spectroscopy of Thermally Excited Quasiparticles in $YBa_2Cu_3O_{6.99}$. *Phys. Rev. B*, 60:1349, 1999.

[17] P. J. Turner, R. Harris, Saeid Kamal, M. E. Hayden, D. M. Broun, D. C. Morgan, A. Hosseini, P. Dosanjh, G. K. Mullins, J. S. Preston, Ruixing Liang, D. A. Bonn, and W. N. Hardy. Observation of Weak-Limit Quasiparticle Scattering via Broadband Microwave Spectroscopy of a d-Wave Superconductor. *Phys. Rev. Lett.*, 90:1231, 2003.

[18] T. Pereg-Barnea, P. J. Turner, R. Harris, G. K. Mullins, J. S. Bobowski, M. Raudsepp, Ruixing Liang, D. A. Bonn, and W. N. Hardy. Absolute Values of the London Penetration Depth in $YBa_2Cu_30_{6+y}$ Measured by Zero Field ESR Spectroscopy on Gd Doped Single Crystals. *Phys. Rev. B*, 69:184513, 2004.

[19] Vespel SP-22 was procured from DuPont, Newark, DE, USA.

[20] O. V. Lounasmaa. *Experimental Principles and Methods Below 1 K.* Academic Press, Inc., London, 1974.

[21] M. Locatelli, D. Arnaud, and M. Routin. Thermal conductivity of some insulating materials below 1 k. *Cryogenics*, 16:374, 1976.

[22] M. A. R. Gunston. *Microwave Transmission-Line Impedance Data.* Van Nostrand Reinhold, London, 1971.

[23] J. R. Pyle. The cutoff wavelength of the TE_{10} mode in ridged rectangular waveguide of any aspect ratio. *IEEE. Trans. Microwave Theory Tech.*, MTT-14:175, 1966.

[24] R. B. Stephens. Low-Temperature Specific Heat and Thermal Conductivity of Noncrystalline Dielectric Solids. *Phys. Rev. B*, 8:2896, 1973.

[25] Haller-Beeman Assoc. Inc., 5020 Santa Rita Rd., El Sobrante, CA 94803 USA.

[26] Chia-Ren Hu. Midgap Surface States as a Novel Signature for $d_{x_a^2-x_b^2}$-Wave Superconductivity. *Phys. Rev. Lett.*, 72:1526, 1994.

[27] A. Carrington, F. Manzano, R. Prozorov, R. W. Giannetta, N. Kameda, and T. Tamegai. Evidence for Surface Andreev Bound States in Cuprate Superconductors from Penetration Depth Measurements. *Phys. Rev. Lett.*, 86:1074, 2001.

[28] Private communication with D. Broun.

[29] P.J. Hirschfeld, W.O. Putikka, and D.J. Scalapino. Microwave conductivity of d-wave superconductors. *Phys. Rev. Lett.*, 71:3705, 1993.

[30] P.J. Hirschfeld, W.O. Putikka, and D.J. Scalapino. d-wave model for the microwave response of high-t_c superconductors. *Phys. Rev. B*, 50:10250, 1994.

[31] W.N. Hardy, D.A. Bonn, Ruixing Liang D.C. Morgan, and Kuan Zhang. Precision measurements of the temperature dependence of λ in $yBa_2Cu_3O_{6.95}$: Strong evidence for nodes in the gap function. *Phys. Rev. Lett.*, 70:3999, 1993.

[32] D.A. Bonn, S.Kamal, Kuan Zhang, Ruixing Liang, D.J. Baar, E. Klein, and W.N. Hardy. Comparison of the influence of Ni and Zn impurities on the electromagnetic properties of $YBa_2Cu_3O_{6.95}$. *Phys. Rev. B*, 50:4051, 1994.

[33] Patrick A. Lee. Localized states in a d-wave superconductor. *Phys. Rev. Lett.*, 71:1887, 1993.

[34] Louis Taillefer, Benoit Lussier, and Robert Gagnon. Universal heat conduction in $YBa_2Cu_3O_{6.9}$. *Phys. Rev. Lett.*, 79:483, 1997.

[35] Adam C. Durst and Patrick A. Lee. Impurity-induced quasiparticle transport and universal-limit wiedemann-franz violation in d-wave superconductors. *Phys. Rev. B*, 62:1270, 2000.

[36] R.W. Hill, Christian Lupien, M. Sutherland, Etienne Boaknin, D.G. Hawthorn, Cyril Proust, F. Ronning, Louis Taillefer, Ruixing Liang, D.A. Bonn, and W.N. Hardy. Transport in ultraclean $YBa_2Cu_3O_7$: Neither unitary nor born impurity scattering. *Phys. Rev. Lett.*, 92:027001–1, 2004.

[37] M. Dressel, N. Kasper, K. Petukhov, B. Gorshunov, G. Grüner, M. Huth, and H. Adrian. Nature of heavy quasiparticles in magnetically ordered heavy fermions UPd_2Al_3 and UPt_3. *Phys. Rev. Lett.*, 88:186404–1, 2002.

[38] P.J. Hirschfeld, W.O. Putikka, and P. Wölfle. Electromagnetic power absorption by collective modes in unconventional superconductors. *Phys. Rev. Lett.*, 69:1447, 1992.

[39] J.R. Feller, C.-C. Tsai, J.B. Ketterson, J.L. Smith, and Bimal K. Sarma. Evidence of electromagnetic absorption by collective modes in the heavy fermion superconductor UBe_{13}. *Phys. Rev. Lett.*, 88:247005–1, 2002.

[40] F. Wooten. *Optical Properties of Solids.* Academic Press, Inc., New York, 1972.

[41] R. M. Bowley and M. Sánchez. *Introductory Statistical Mechanics.* Oxford University Press, Inc., New York, 1996.

[42] N. W. Ashcroft and N. D. Mermin. *Solid State Physics.* Thomson Learning, Inc., USA, 1976.

Appendix A

Oscillator Strength Sum Rule

In this appendix the expression for the oscillator strength sum rule (Eq. 1.23) found in §1.4 is derived starting from the Kramers-Krönig transformation that relates the real and imaginary parts of causal response functions. This derivation follows that of Wooten [40].

Causality implies that there can be no response before the stimulus. The conductivity $\sigma(\omega) = \sigma_1(\omega) - i\sigma_2(\omega)$ is an example of a causal response function; the electrons cannot respond to an electromagnetic field until that field has been applied. The Kramers-Krönig transformation required for the purposes of this appendix is:

$$\sigma_2(\omega_o) = \frac{2}{\pi} P \int_0^\infty \frac{\omega_o}{\omega^2 - \omega_o^2} \sigma_1(\omega)\, d\omega, \tag{A.1}$$

where P stands for the principal value of the integral. We proceed by separating the above integral as follows:

$$\sigma_2(\omega_o) = \frac{2}{\pi} P \int_0^{\omega_c} \frac{\omega_o}{\omega^2 - \omega_o^2} \sigma_1(\omega)\, d\omega + \frac{2}{\pi} P \int_{\omega_c}^\infty \frac{\omega_o}{\omega^2 - \omega_o^2} \sigma_1(\omega)\, d\omega, \tag{A.2}$$

where a cut-off frequency ω_c has been inserted. The cut-off frequency is defined such that $\sigma_1(\omega) = 0$ for $\omega > \omega_c$, that is, there is no absorption for frequencies above ω_c. If we are interested in $\sigma_2(\omega_o)$ for $\omega_o \gg \omega_c$ Eq. A.2 reduces to:

$$\sigma_2(\omega_o) \approx \frac{2}{\pi} \frac{1}{\omega_o} \int_0^\infty \sigma_1(\omega)\, d\omega, \qquad \omega_o \gg \omega_c. \tag{A.3}$$

The upper integration limit has been restored to ∞ because $\sigma_1(\omega) = 0$ for frequencies above ω_c. Next the real part of the conductivity is written as a sum of superfluid and normalfluid contributions, $\sigma_1(\omega) = \sigma_{1s}(\omega) + \sigma_{1n}(\omega)$. The superfluid part can be integrated using Eq. 1.21 so that Eq. A.3 becomes:

$$\sigma_2(\omega_o) \approx \frac{1}{\omega_o} \frac{n_s e^2}{m^\star}(T) + \frac{2}{\pi} \frac{1}{\omega_o} \int_0^\infty \sigma_{1n}(\omega)\, d\omega. \tag{A.4}$$

At sufficiently high frequencies the electrons can be considered as free and the conductivity is well described by the Drude model. Recalling Eqs. 1.17 we have $\sigma_2(\omega_o) \approx ne^2/m^\star\omega_o$ for large ω_o. Combining this result with Eq: A.4 produces desired sum rule:

$$\frac{ne^2}{m^\star} - \frac{n_s e^2}{m^\star}(T) = \frac{n_n e^2}{m^\star}(T) \approx \frac{2}{\pi} \int_0^\infty \sigma_{1n}(\omega, T)\, d\omega. \tag{A.5}$$

Appendix B

Heat Capacity of Copper

The stainless steel/copper filters discussed in chapter 5 must be cooled from room temperature down to temperatures as low as 50 mK. To calculate the cooling rate of the filters one must have detailed knowledge of the temperature dependent heat capacity $C_V(T)$ of copper. There is a phononic contribution to the heat capacity which dominates at high temperature and an electronic contribution that becomes important below $\sim$ 10 K.

In 1912 Debye presented a quantum mechanical treatment of vibrations in a solid which was a generalization of Einstein's 1907 treatment. Debye assumed that all vibrational modes reside below some cut-off frequency ω_D (now termed the Debye frequency). Enforcing this requirement led Debye to the following expression for the phonon contribution to the heat capacity:

$$C_V = 9k_B N \left(\frac{T}{\theta_D}\right)^3 \int_0^{\theta_D/T} \frac{x^4 e^x}{(e^x - 1)^2} dx, \tag{B.1}$$

where there are N atoms in the lattice, $\theta_D = \hbar\omega_D/k_B$ is the Debye temperature and $x = \hbar\omega/k_B T$. When compared to experimental data for copper this expression fits the data extremely well over almost the entire temperature range with a Debye temperature of $\theta_D = 342$ K. There is however, a discrepancy between the theory and data for temperatures below 10 K and is due to the thermal activation of conduction electrons. At low temperatures the Debye model predicts that $C_V \propto T^3$ in contrast to the observed linear temperature dependence. [41]

For finite temperatures well below the Fermi temperature particles within $k_B T$ of the Fermi energy are excited to unoccupied states just above the Fermi energy. This thermal activation of electrons leads to an additional electronic contribution to the heat capacity given by:

$$C_V = \frac{N k_B \pi^2}{2} \left(\frac{k_B T}{E_F}\right). \tag{B.2}$$

The Fermi energy of copper is 7.04 eV leading to an electronic specific heat per unit mass of $c_V = 8.0 \times 10^{-3}$ $JK^{-1}kg^{-1}$ [42]. Fig. B.1 is a plot of the specific heat per unit mass of copper as a function of temperature highlighting the importance of the electronic contribution at low temperatures. As the temperature is increased the specific heat is quickly dominated by phonons.

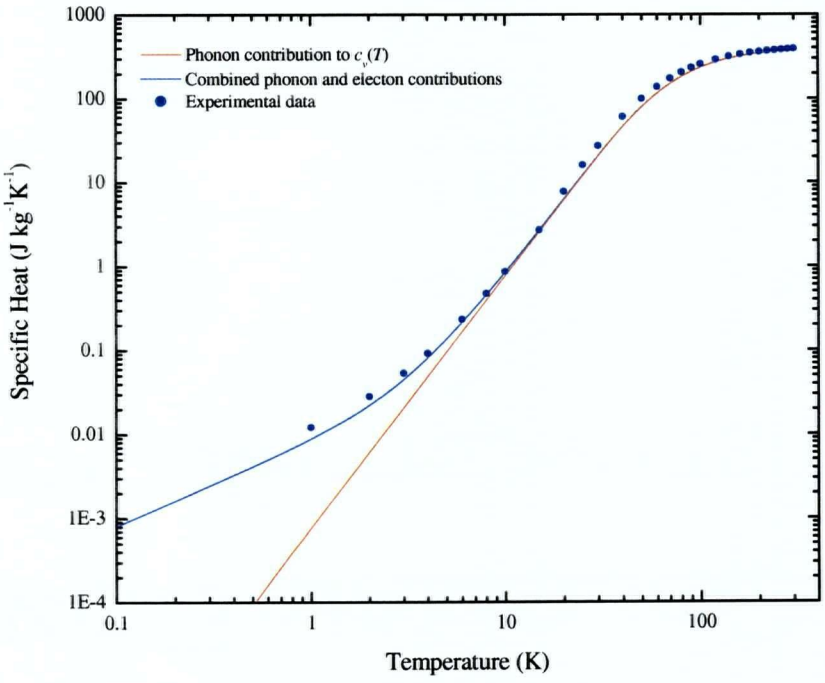

Figure B.1: Specific heat per unit mass of copper plotted as a function temperature on a log-log scale. The red curve is the Debye approximation for the phonon contribution and the blue curve includes the electron specific heat assuming E_F=7.04 eV. The data points are experimental data taken from reference [2].